Vertical Motions Forced by Small-Scale Terrain and Cloud Microphysical Response in Extratropical Precipitation Systems

Bart Geerts, a Coltin Grasmick, a Robert M. Rauber, b Troy J. Zaremba, b Lulin Xue, c and Katja Friedrich $^{\rm d}$

a Department of Atmospheric Sciences, University of Wyoming, Laramie, Wyoming
b Department of Atmospheric Sciences, University of Illinois at Urbana–Champaign, Urbana, Illinois
c National Center for Atmospheric Research, Boulder, Colorado
d Department of Atmospheric and Ocean Sciences, University of Colorado Boulder, Boulder, Colorado

(Manuscript received 21 July 2022, in final form 30 October 2022)

ABSTRACT: Airborne vertically profiling Doppler radar data and output from a ~1-km-grid-resolution numerical simulation are used to examine how relatively small-scale terrain ridges (~10-25 km apart and ~0.5-1.0 km above the surrounding valleys) impact cross-mountain flow, cloud processes, and surface precipitation in deep stratiform precipitation systems. The radar data were collected along fixed flight tracks aligned with the wind, about 100 km long between the Snake River Plain and the Idaho Central Mountains, as part of the 2017 Seeded and Natural Orographic Wintertime clouds: the Idaho Experiment (SNOWIE). Data from repeat flight legs are composited in order to suppress transient features and retain the effect of the underlying terrain. Simulations closely match observed series of terrain-driven deep gravity waves, although the simulated wave amplitude is slightly exaggerated. The deep waves produce pockets of supercooled liquid water in the otherwise ice-dominated clouds (confirmed by flight-level observations and the model) and distort radar-derived hydrometeor trajectories. Snow particles aloft encounter several wave updrafts and downdrafts before reaching the ground. No significant wavelike modulation of radar reflectivity or model ice water content occurs. The model does indicate substantial localized precipitation enhancement (1.8–3.0 times higher than the mean) peaking just downwind of individual ridges, especially those ridges with the most intense wave updrafts, on account of shallow pockets of high liquid water content on the upwind side, leading to the growth of snow and graupel, falling out mostly downwind of the crest. Radar reflectivity values near the surface are complicated by snowmelt, but suggest a more modest enhancement downwind of individual ridges.

SIGNIFICANCE STATEMENT: Mountains in the midlatitude belt and elsewhere receive more precipitation than the surrounding lowlands. The mountain terrain often is complex, and it remains unclear exactly where this precipitation enhancement occurs, because weather radars are challenged by beam blockage and the gauge network is too sparse to capture the precipitation heterogeneity over complex terrain. This study uses airborne profiling radar and high-resolution numerical simulations for four winter storms over a series of ridges in Idaho. One key finding is that while instantaneous airborne radar transects of the cross-mountain flow, vertical drafts, and reflectivity contain much transient small-scale information, time-averaged transects look very much like the model transects. The model indicates substantial surface precipitation enhancement over terrain, peaking over and just downwind of individual ridges. Radar observations suggest less enhancement, but the radar-based assessment is uncertain. The second key conclusion is that, even though orographic gravity waves are felt all the way up into the upper troposphere, the orographic precipitation enhancement is due to processes very close to the terrain.

KEYWORDS: Mixed precipitation; Orographic effects; Radars/Radar observations; Numerical analysis/modeling

1. Introduction

Precipitation from midlatitude frontal systems is often enhanced over complex terrain (e.g., Douglas and Glasspoole 1947; Roe 2005). Attention generally has focused on large mountain ranges, such as the Sierra Nevada, where the time scale of precipitation growth and fallout typically is small compared to the advective time scale over the main crest, but recent studies have shown higher seasonal precipitation totals even for relatively small-scale ridges, compared to nearby valleys. For instance, Minder et al. (2008) document 50%–70% more annual precipitation over ~800-m-high ridges just

of the Olympic Mountains in the northwestern United States. Similar O(10)-km-scale enhancements have been documented elsewhere, including in Northern California (Neiman et al. 2002), central Chile (Garreaud et al. 2016; Massmann et al. 2017), and southern Norway (Barstad and Caroletti 2013). An obvious thermodynamic factor explaining the precipita-

 \sim 10 km wide, relative to the adjacent valleys, on the coastal side

An obvious thermodynamic factor explaining the precipitation variation across small-scale terrain undulations is the cloud-base height above ground level, and differential evaporation of precipitation below cloud base between ridges and valleys. This factor probably is important in all four examples above, because they are all coastal ranges with relatively warm surface conditions. Several dynamical processes may also affect this variation. These include the presence of potential instability, which may be released by ascent over a

Corresponding author: Bart Geerts, geerts@uwyo.edu

DOI: 10.1175/JAS-D-22-0161.1

mountain ridge (e.g., Kirshbaum and Durran 2004), leading to convective precipitation over and downwind of the triggering ridge. Terrain-driven vertically propagating gravity waves in stratified flow may also modulate hydrometeor growth (Reinking et al. 2000; Garvert et al. 2007; Zagrodnik et al. 2021). Such terrain-driven gravity wave motions are commonly seen in high-resolution model output, including operational weather models, but they are difficult to observe.

Whatever causes small-scale orographic precipitation variations, numerical weather prediction model simulations appear to skillfully simulate seasonal precipitation patterns as long as the models are sufficiently resolved (e.g., Minder et al. 2008; Garreaud et al. 2016; Ikeda et al. 2010), although major discrepancies may exist for individual storms (e.g., Prein et al. 2013). Moreover, recent modeling work has brought into question the accuracy of gauge-based, gridded precipitation datasets such as the 800-m-resolution Parameter-Elevation Regressions on Independent Slopes Model (PRISM) product (Daly et al. 2008) over complex terrain (e.g., Jing et al. 2017; Lundquist et al. 2019), including over small-scale terrain features.

This study focuses on data collected in February/March 2017 as part of the Seeded and Natural Orographic Wintertime clouds: the Idaho Experiment (SNOWIE; Tessendorf et al. 2019). SNOWIE targeted a mountainous part of Idaho, with multiple closely spaced (~10-25 km) terrain ridges (Fig. 1). For reference, the 30 yr, 800 m PRISM precipitation normals are mapped over the SNOWIE domain in Fig. 1c, over the 2 months of relevance. Within this domain, there are just eight Snowpack Telemetry (SNOTEL) sites (Serreze et al. 1999) (Fig. 1c). SNOTEL sites are the primary source of precipitation data for the PRISM product in this region. The PRISM precipitation distribution is terrain-dependent statistical estimate: precipitation increases from the Snake River basin in the west to the Central Mountains in the east; superimposed on this trend are maxima roughly collocated with the terrain ridges in the Payette River basin (Fig. 1c).

This study uses data from an airborne profiling Doppler radar, the Wyoming Cloud Radar (WCR), combined with a Weather Research and Forecasting (WRF) Model simulation with a grid resolution of ~1 km, to examine how vertical motions may influence precipitation distributions across ridges that are 10-25 km apart. WCR transects collected along straight and level flight legs over the SNOWIE domain (Fig. 1b) and elsewhere during the passage of baroclinic disturbances show many small-scale (~1-km-width) vertical velocity patterns that are mobile and transient, i.e., they are present in one transect but not in the next: transient patterns include embedded convection (e.g., Chu et al. 2017) and Kelvin-Helmholtz waves (e.g., Grasmick and Geerts 2020; Cann et al. 2022). Such transects also include terrain-driven vertical drafts (e.g., Geerts et al. 2015; French et al. 2015; Kingsmill et al. 2016). The superposition of multiple geographically fixed WCR-derived vertical velocity transects suppresses the transient signal and elevates the stationary, terrain-driven component (Zaremba et al. 2022b). Here, we examine four examples of such "composite" WCR transects, collected on a fixed track aligned with the mean wind near flight level, flown repeatedly, back and forth. We then contrast the WCR-observed velocity and reflectivity patterns against those obtained from the high-resolution WRF simulation. An additional factor to be considered in these composites is the evolving synoptic situation during the \sim 3 h of WCR data collection, since each of the four cases sampled a frontal disturbance.

The objective of this study is to document terrain-induced vertical velocity patterns over terrain with multiple mesoscale ridges, and to examine how these vertical motions alter liquid water content, hydrometeor growth, and precipitation. The focus is on processes, not the climatology. Section 2 describes the data and observational methods. Section 3 describes the composite vertical velocity structure for the four cases, and examines how these vertical velocities alter cloud and precipitation. A discussion follows in section 4, and key findings are summarized in section 5.

2. Data and methods

a. The Wyoming King Air

This study uses data collected during SNOWIE, in which the University of Wyoming King Air (UWKA) flew repeatedly back and forth along fixed, straight tracks. The aircraft collected profiling radar data and in situ cloud microphysical and meteorological data. Here, we use liquid water content (LWC) and ice water content (IWC) measurements from a Nevzorov probe (Korolev et al. 2013). For the four flights examined here, the Nevzorov LWC measurement compares well to LWC estimates from another probe, the Cloud Droplet Probe, where droplet water mass is integrated over the size spectrum from 2 to 50 µm. This comparison uses both scatterplots and histograms (not shown); mean values of the two probes are within 35% of the overall mean. The aircraft did not carry an independent bulk IWC probe, so the Nevzorov IWC estimate is less certain, but Korolev et al. (2013) report that for ice particles smaller than 4 mm, the Nevzorov IWC falls within 50% of IWC estimates from two other probes.

In situ air vertical velocity (w) estimates are from a gust probe. Because gust probe velocity components result from the integration of accelerations, their variations are more accurate than their long-track mean. For the four research flights (RFs) in this study, the tracks are ~100 km long, and the leg-average w values are -0.21, 0.14, 0.01, and -0.39 m s^{-1} on average, with standard deviations of 0.08, 0.10, 0.11, and 0.64 m s⁻¹, respectively. It is customary for boundary layer studies to remove the average (\overline{w}) over a sufficiently long straight and level flight leg (e.g., Lenschow 1972; Geerts and Miao 2005), such that $\overline{w} = 0$. Here, we do the same and examine the flight-level perturbation air vertical velocity, $w' = w - \overline{w}$, which is accurate to 0.1 m s^{-1} ; w' can be interpreted as air vertical velocity only if the track-mean value \overline{w} is negligible. This may not be the case in the orographic cloud systems examined here. This question is addressed below.

The two main tracks used in SNOWIE were track A (100 km long), flown under westerly winds, and track B (110 km long), flown under southwesterly winds (Fig. 1b). Here, we use data from two RFs along track A (RF11 on

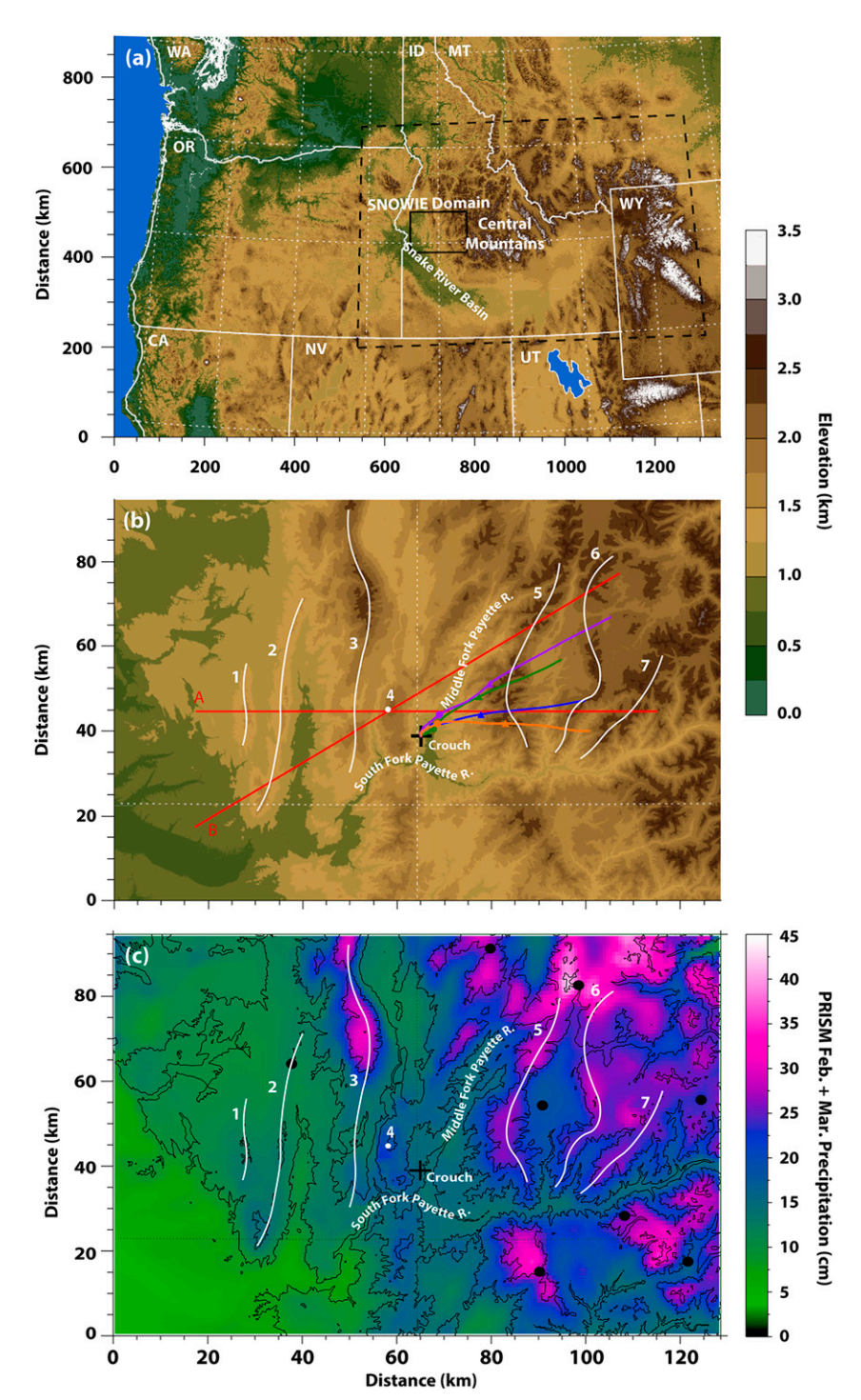


FIG. 1. Terrain maps. (a) Large-scale domain containing the 900-m-resolution model domain (dashed black rectangle) and the SNOWIE observational domain (solid black rectangle). (b) SNOWIE observational domain with labels marking ridges and valleys mentioned in the text, and the two flight tracks flown repeatedly during SNOWIE in red. The Crouch rawinsonde launch location is noted by the black cross. The colored lines indicate the ascent path of the rawinsonde for IOP-23 (orange), IOP-11 (blue), IOP-24 (green), and IOP-17 (purple) between the surface and 9 km MSL. Rawinsonde altitudes of 3 and 6 km MSL are identified by solid circles and triangles, respectively, along this path. (c) Average 30 yr (1991–2020) cumulative precipitation for February and March, from PRISM. The black circles are the locations of the SNOTEL sites. Elevation is contoured every 500 m. In (b) and (c), terrain ridges of interest are highlighted with white lines and numbered as follows: 1) West Squaw Butte; 2) East Squaw Butte; 3) Western Range; 4) Packer John; 5) West Salmon River Range; 6) Central Salmon River Range; 7) East Salmon River Range.

4 February and RF23 on 9 March) and from two RFs along track B (RF17 on 21 February and RF24 on 16 March). These two tracks are shown in Fig. 1b. These RFs are chosen for the presence of deep stratiform cloud, the number of repeat flight legs, and the quality of the measurements.

b. The Wyoming Cloud Radar

In all SNOWIE flights, the UWKA carried the WCR, a W-band pulsed Doppler radar (Wang et al. 2012), with three fixed antennas: One pointing up, one pointing down, and one pointing slant forward, 30° from nadir. The W-band power is attenuated by liquid water along the ray path, at a rate of ~9.2 dB km⁻¹ (g m⁻³)⁻¹ of cloud droplets at representative temperatures (Vali and Haimov 2001). For this study, the two key WCR-derived variables are air vertical velocity (up and down), and along-track wind (below flight level only).

The hydrometeor vertical velocity is derived from the WCR nadir/zenith antenna Doppler velocity, following a series of corrections related to aircraft motion, aircraft attitude (pitch, roll, and yaw), and known antenna beam pointing vectors on the aircraft. We also remove the estimated contamination of the horizontal wind into the quasi-vertical beam using the known beam pointing vector, as detailed in Zaremba et al. (2022a) and references therein. The hydrometeor vertical velocity (w_H) is the sum of air vertical velocity (w) and the (negative) hydrometeor fall speed (V_T) . Following Zaremba et al. (2022a), we assume that, averaged over the length of the full flight track (~100 km long), $\overline{w} = 0$. It then follows that, at any height z above ground level (AGL), the track-average $\overline{w_H} = \overline{V_T}$, where the overbars indicate horizontal averages, so $\overline{V_T}$ depends on height AGL only. If we further assume that at a given height the fall speed is invariant $(V_T = \overline{V_T})$, then the local value for the WCR-derived perturbation w' equals $w' = w_H - \overline{V_T}$. The same symbol w' is used for gust probe and WCR data, since it regards the same parameter (air vertical motion), under the same assumption. The analysis below examines composite fields of both w_H and w'. If the freezing level (where slow-falling snow transitions to fast-falling rain) is not level along the track, then, because the leg-average $\overline{V_T}$ is subtracted, the w' field will contain some anomalies unrelated to vertical air motion, rendering w' meaningless within the height range of melting levels in the transect. In addition, the $\overline{w} = 0$ assumption loses validity toward the highest cloud tops and in valleys, or in general at levels where there are few data points to average, resulting in larger uncertainty in w' (Zaremba et al. 2022a). Zaremba et al. (2022a) evaluate the uncertainties in the WCR-based estimation of w'. They partition the total uncertainty in its components, i.e., each of the three assumptions made in the derivation discussed above: 1) that at a given height the horizontal wind is invariant, 2) that at a given height the leg-mean $\overline{w} = 0$, and 3) that at a given height V_T is invariant. The total vertically averaged uncertainty for the four cases examined herein ranges between 0.14 and -0.23 m s^{-1} and is dominated by assumption 3. For more details, we refer the reader to Zaremba et al. (2022a).

By combining the WCR nadir and slant-forward beams, dual-Doppler synthesis is used to derive the 2D wind field

(along track, vertical) in a vertical plane below the UWKA, following a technique first developed by Damiani and Haimov (2006). This technique has been used in many other studies, including Grasmick and Geerts (2020). Uncertainties impacting airborne dual-Doppler synthesis are discussed in Damiani and Haimov (2006): Errors are due mainly to the cross-track advection of scatterers, aircraft attitude changes, and beampointing vector uncertainties. The UWKA flew roughly parallel with the wind at flight level in SNOWIE, implying that it did not need to "crab" into the wind to stay on the geographically fixed track. This reduces the synthesis uncertainty, as the nadir and the slant forward beams are aligned along the track. Additionally, the errors typically introduced by small-scale changes in wind speed and direction are greatly reduced by compositing the dual-Doppler wind. In short, the average along-track flow is measured accurately. We note that during most SNOWIE RFs, including the four RFs used herein, the wind generally veered with height at low levels, implying a low-level cross-track component. The implications of this cross-track wind component will be discussed below.

WCR data are composited along quasi-overlapping flight tracks. Sideways departures from the set track are small (<1 km generally). WCR data are binned first as a function of distance (~400 m) and height (30 m), and then averaged. The precise bin width is 0.0050° longitude for track A (corresponding with 399 m) and 0.0041° longitude for track B (~397 m). This averaging suppresses transient features in the flow and reflectivity fields and retains terrain-induced patterns. Reflectivity is averaged linearly in units of mm⁶ m⁻³. Each case has about 10 flight transects. Sometimes the end point was cut short, i.e., the aircraft was turned around before reaching the designated end point, resulting in some data loss at the eastern and western margins. The composite fields also contain fewer data near flight level: the WCR blind zone is 250 m deep, combining up and down antennas. This issue is mitigated by the multiple flight levels flown on the fixed tracks in each of the four cases, as shown below.

c. Rawinsonde data

For each of the four cases, data from a rawinsonde (type: Lockheed Martin LMS6) launched just before the middle of the flight period from Crouch, Idaho (Fig. 1b), were used to describe thermodynamic conditions. The rawinsonde data had an average vertical resolution of 4 m and drifted an average of 20 km away from their launch location between the surface and cloud top, for the four RFs used herein, with little case-to-case variation (Fig. 1b). For both track A cases, for instance, the balloon traveled up the Middle Fork Payette River valley for a few kilometers, and then ascended roughly along track A (Fig. 1b).

Several thermodynamic variables are derived from the sounding data: the equivalent potential temperature θ_e (K), the Brunt–Väisälä (BV) frequency N (s⁻¹), and the Scorer parameter ℓ^2 (m⁻²). N is computed as the dry BV frequency below the lifting condensation level (LCL), and the moist BV frequency, calculated as in Kirshbaum and Durran (2004), above the LCL. The LCL is quite low (below 500 m AGL) in

all cases examined herein, so effectively N is the moist Brunt–Väisälä frequency. The Scorer parameter is defined as

$$\ell^2 = \frac{N^2}{U^2} - \frac{\frac{\partial^2 U}{\partial z^2}}{U},\tag{1}$$

where U(z) is the cross-mountain wind speed, and z is the vertical distance. Since the mountain ridges of interest are essentially north-to-south oriented, U(z) is the zonal wind profile. Rawinsonde data used for the calculation of N and ℓ^2 were interpolated to a 20 m resolution grid using the spline method and then smoothed by a 100-m-deep moving average. The condition $\ell^2 < 0$ is favorable for gravity wave trapping (Crook 1988).

d. WRF Model configuration

In support of SNOWIE research, the WRF Model version 3.9.1.1 was run continuously starting on 1 October 2016 and ending on 30 April 2017, encapsulating the SNOWIE field phase. The simulations used a $\Delta x = 2700$ m outer domain and a $\Delta x = 900$ m nested inner domain (outlined in Fig. 1a), with 81 terrain-following vertical levels (eta coordinates) between the surface and 20 hPa. The levels were distributed densely at low levels, with 23 levels below 1 km AGL, and 43 levels below 3 km AGL. Initial and boundary conditions for the WRF simulation are from the 6-hourly 3D ERA-Interim dataset, which has a resolution of $0.75^{\circ} \times 0.75^{\circ}$. The model configuration is summarized in Tessendorf et al. (2019) and in Zaremba et al. (2022b). Key parameterization choices are the Noah Multi-Physics land surface scheme (Niu et al. 2011), which tracked soil moisture and snowpack throughout the season, the Mellor-Yamada-Nakanishi-Niino scheme (MYNN) planetary boundary layer (PBL) scheme (Nakanishi and Niino 2004), and the Thompson-Eidhammer (Thompson and Eidhammer 2014) cloud microphysics scheme. Hourly WRF Model output of vertical motion fields and cloud-related variables along the flight tracks was composited to enable timespace-matched comparisons between the model and the rawinsonde, WCR, and in situ observations, with an effective $(\delta t, \delta x, \delta z)$ tolerance of (30 min, 500 m, 100 m). The closest four model bins were interpolated to any WCR grid point.

3. Composite vertical velocity structure

a. Track A: Research flight 23: Kinematics

A broad ridge was present over the Pacific Northwest ahead of a deep trough on 9 March 2017 (Fig. 2a). Research flight 23 was flown during a period of low-level warm-air advection ahead of a NW-SE-oriented frontal boundary, analyzed at the surface as a warm front across Idaho just north of track A (Fig. 2b). A vertical transect along track A, extending from just off the Oregon coast to NW Wyoming, shows a deep moist air mass (~10 km deep) with isentropically ascending moisture transport from the Pacific across the length of the transect (Fig. 3a). While this moist air mass was weakly stratified at most levels (Fig. 3a), the flow was more stratified below 2.0 km AGL, at least at Crouch (Figs. 4a,e), located in a somewhat enclosed basin (Fig. 1b). In the Payette River

basin around Crouch, low-level flow was southerly (Fig. 4n, and wind profiles shown in the upper left in Fig. 4). The lowlevel stratification, the low-level southerly flow from the Snake River plain, and the strong wind shear near mountain top level (Fig. 4i) all are indicative of flow blocking (Froude number Fr < 1), which was observed in three of the four cases examined here (Table 1) and during many SNOWIE intensive observation periods (Tessendorf et al. 2019). These features had been stronger earlier in the day, and were weaker by the flight period (around 2100 UTC) as the frontal boundary receded poleward, but colder air remained in mountain valleys, such as at Crouch (Fig. 4c). Across Idaho, including along track A, a deep terrain-driven gravity wave signature is evident in the model relative humidity (RH) transect (Fig. 3a). In this region, the $\Delta x = 2700$ m model output shows a strong correlation between RH and vertical velocity, with RH maxima located just downstream of updraft peaks (not shown).

The 15-panel plot in Fig. 4 shows both WCR/rawinsonde observations and WRF inner domain ($\Delta x = 0.9 \text{ km}$) model output for RF23 (nine transects; see Table 1). The model output is available hourly at the top of the hour. The model fields shown are the average from the 3 hourly model output times that bracket the nine transects. The length of the WCR cross section in Fig. 4 is slightly less than the 100 km mention in section 2a, to focus on the region with the most overlapping transects.

For each individual transect, the $\overline{V_T}$ profile is subtracted from the hydrometeor vertical velocity (w_H) to obtain the air vertical velocity (w'). The 9-transect mean $\overline{V_T}$ profile for RF23 is shown in Fig. 5, and the composite w_H and w' are shown in Figs. 4f and 4g, respectively. As already shown by Zaremba et al. (2022b) for all SNOWIE flights along track A, the composite w_H (Fig. 4f) and w' (Fig. 4g) fields reveal patterns that clearly are related to the underlying terrain. Track A intersects 7 ridges (marked below Fig. 4f and labeled in Fig. 1b), and each one is marked by a vertical velocity dipole, with ascent on the west and descent on the east. The vertical velocity dipole is strongest for the widest, tallest ridge (5), peaking at +1.3 and -1.7 m s⁻¹ at 4 km MSL (Fig. 4g). Two rather sharp ridges (4 and 5) also produce a shallow, evanescent vertical velocity dipole, with extrema just a few kilometers apart.

The "surprising" low-level updraft just east of ridge 2 may be attributable to the southerly upslope flow in that valley (Fig. 2b), anticipated based on the Crouch observed and modeled wind profiles (Fig. 4), and the model meridional wind (Fig. 4n). On the other hand, the "surprising" deep updraft above the Middle Fork Payette River valley just east of ridge 4 (Packer John) most likely is a resonant response (trapped lee wave) triggered by ridge 4: Given that between 4 and 6 km MSL, where the wave ascent is strongest, $U \sim 23 \text{ m s}^{-1}$, and $N \sim 6 \times 10^{-3} \text{ s}^{-1}$ (Figs. 4a,d), the half-wavelength of

¹ During RF23, the melting layer was tilting down toward the east (Fig. 4f), from 2.5 km on the west side to 2.1 km in the high valleys on the east side. This slope, which persisted throughout the flight, explains the erroneous radar-retrieved w'; pattern near the freezing level in Fig. 4g (section 2b).

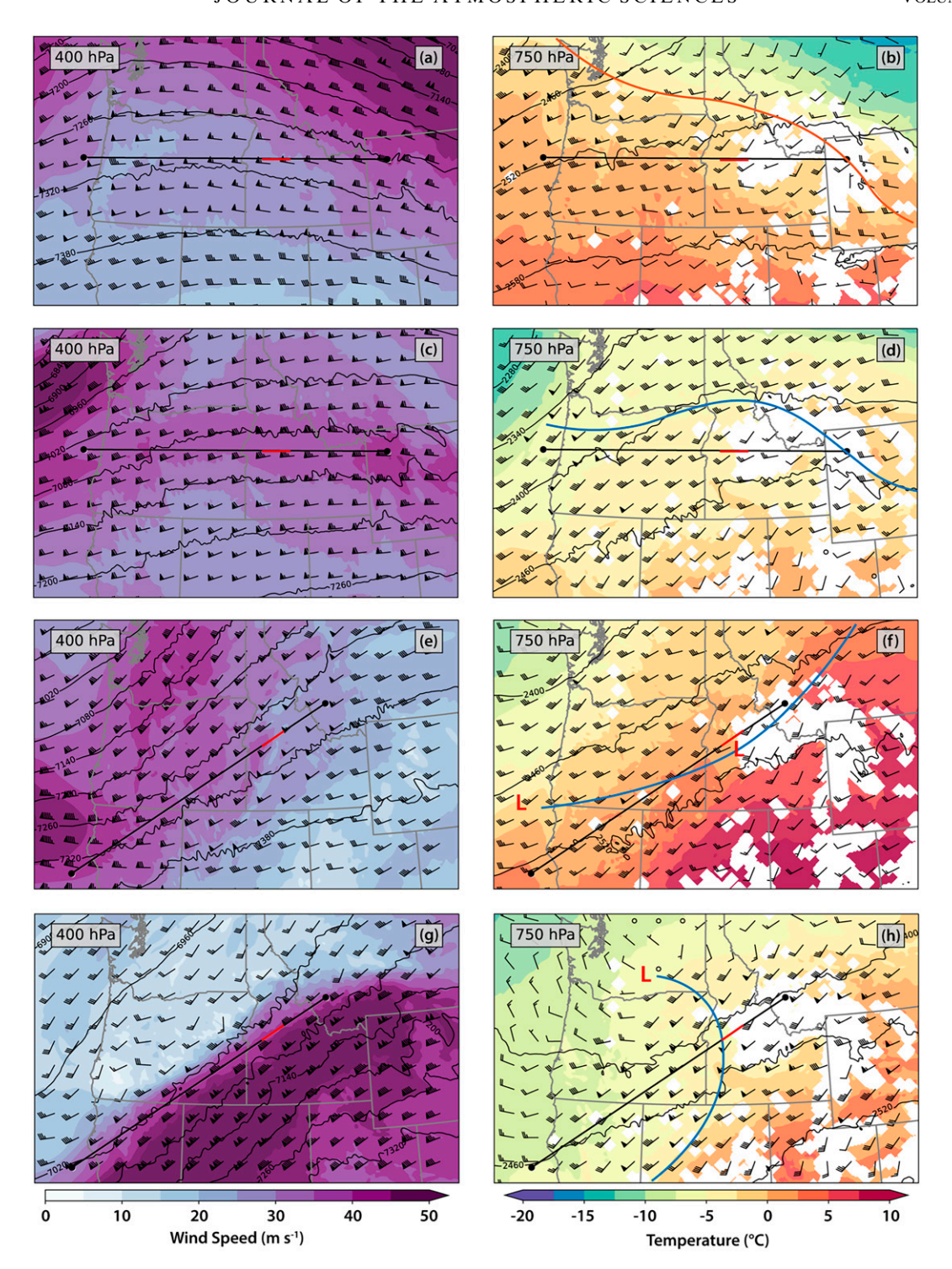


FIG. 2. Synoptic analysis for the four cases examined herein, based on the outer domain ($\Delta x = 2.7$ km) WRF simulation. (left) 400 hPa geopotential height (contours), wind speed (color), and wind barbs. (right) 750 hPa height (contours), temperature (color), and wind barbs. (a),(b) 2100 UTC 9 Mar 2017, during RF23; (c),(d) 2300 UTC 4 Feb, during RF11; (e),(f) 0200 UTC 16 Mar, during RF24; (g),(h) 1600 UTC 21 Feb, during RF17. The black lines indicate the location of the vertical transects in Fig. 3, and the short red sections in these lines indicate the UWKA flight track. The right panels include a surface weather analysis, including frontal boundaries (red for warm fronts, blue for cold fronts) and the location of the surface low. No temperature data are shown where the 750 hPa surface dips below the terrain.

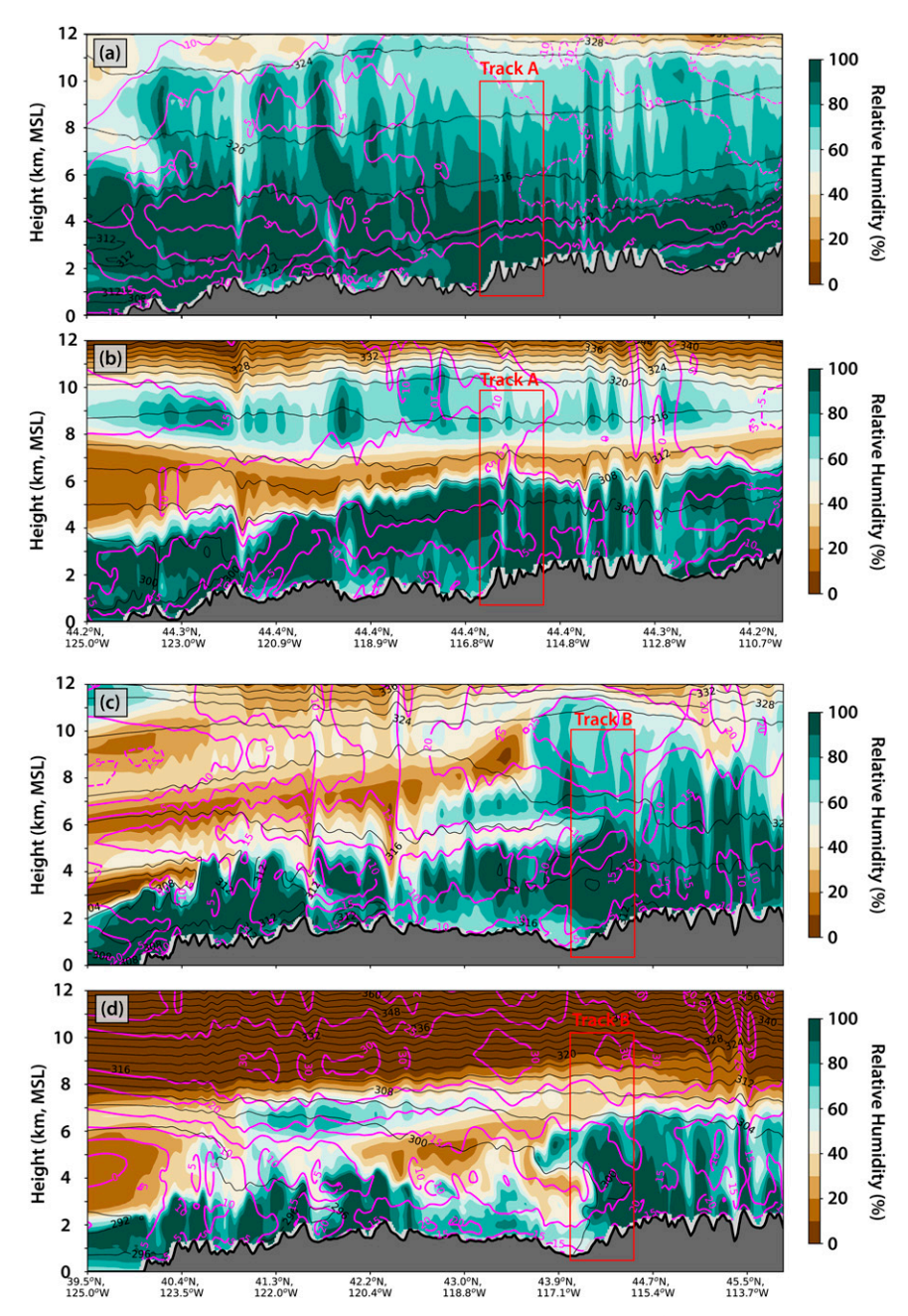


FIG. 3. Cross sections of meridional wind (magenta contours, m s⁻¹, positive solid, negative dashed) overlain on relative humidity with respect to water (color fill, %). The thin black contours are θ_e (K). The location of the transect is shown in Fig. 2. The dates and times match those in Fig. 2 for the four cases: (a) RF23; (b) RF11; (c) RF24; (d) RF17. Data source: Outer domain $(\Delta x = 2.7 \text{ km})$ WRF simulation.

such wave would be about 14 km ($\pi U/N$), which is about the distance between the downdraft and subsequent updraft in the lee of ridge 4. The strongest, deepest, and widest updraft can be found just west (upstream) of ridge 6 (Fig. 4g). This also may be attributed to a lee-wave response to the strongest downdraft in the transect, just east of ridge 5, positively interfering with the upslope terrain toward ridge 6.

The WRF simulation reproduces the 2D structure of vertical velocity remarkably well (Fig. 4l), including the vertical propagation properties, the strong gravity wave response to ridges 5 and 6, and even two lee-wave updrafts found over valleys. [Note that the model output is w, not w', i.e., we did not subtract $\overline{w}(z)$.] The model does not resolve the smaller-scale shallow evanescent waves around the ridge crests 4 and 5.

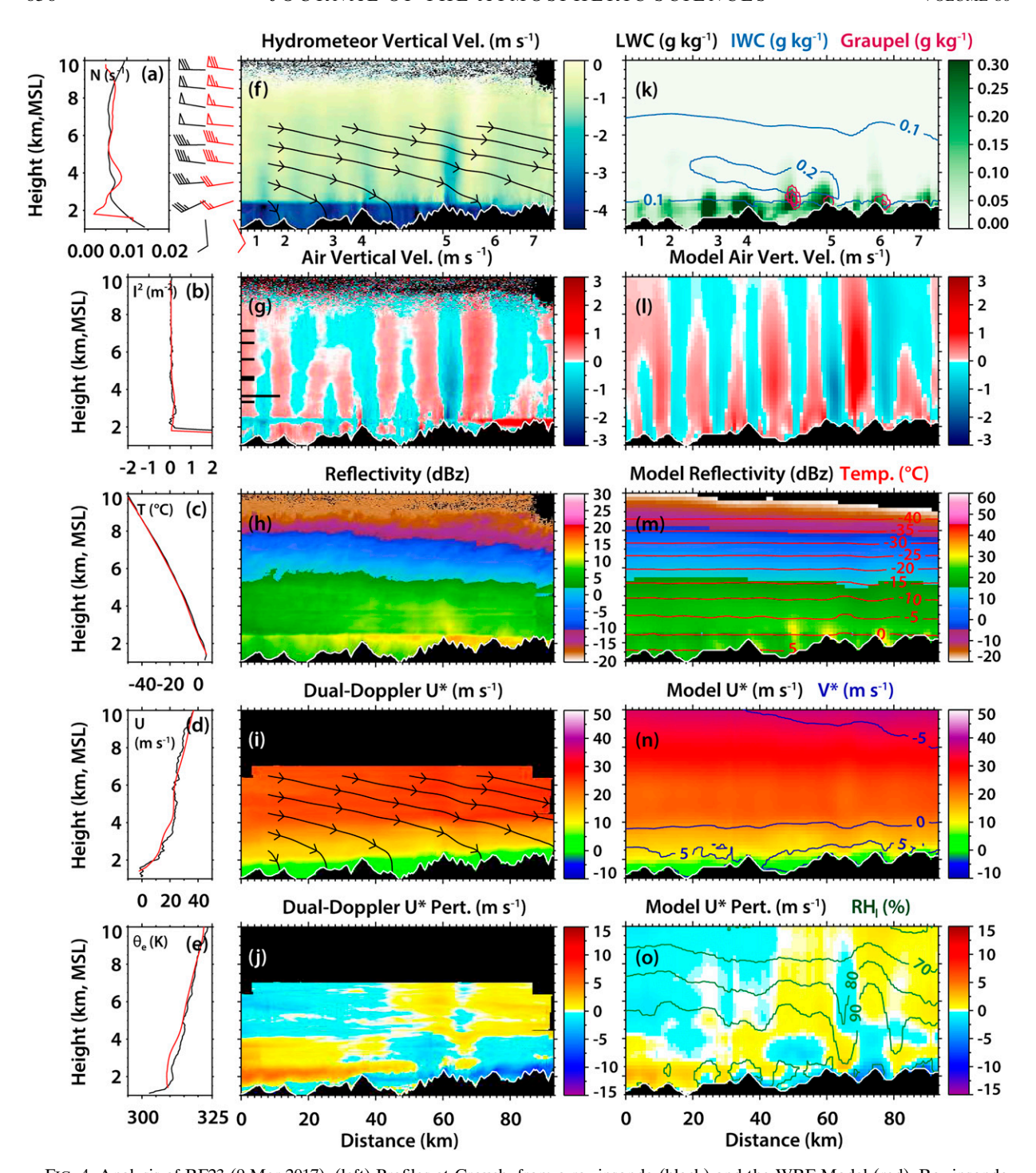


FIG. 4. Analysis of RF23 (9 Mar 2017). (left) Profiles at Crouch, from a rawinsonde (black) and the WRF Model (red). Rawinsonde (black) and model (red) wind profiles (barbs) are shown to the right of (a). (center) WCR-derived fields. (right) WRF Model-based fields. (a) Brunt-Väisälä frequency $N(s^{-1})$; (b) Scorer parameter ℓ^2 (m⁻²); (c) temperature $T(^{\circ}C)$; (d) zonal wind $U(ms^{-1})$; (e) equivalent potential temperature $\theta_e(K)$; (f) WCR hydrometeor vertical velocity w_H ; (g) air vertical velocity w'; (h) W-band reflectivity; (i) along-track wind u^* ; (j) departure from the mean along-track wind profile u^*' ; (k) model LWC (cloud water and rain) (color fill), snow + cloud ice (blue contours), and graupel (magenta contours, 0.1 g kg⁻¹ interval); (l) model w; (m) model reflectivity (color fill) and T (contours); (n) model u^* (color fill) and across-track wind v^* (contours); and (o) model u^* (color fill) and relative humidity (RH) relative to liquid (contours). WCR-derived hydrometeor streamlines [based on (u^*, w_H)] are drawn in (f) and (i). The terrain ridges of interest are numbered below (f) and (k) as in Fig. 1b. The distribution of UWKA flight levels is shown on the left border of (g) as "tick marks." A single 4-km-long tick mark corresponds to one traverse at that level.

TABLE 1. Summary evaluation of WRF simulation against observations (obs). All data are based on the composite information shown in figures in this paper.

Variable	Units	2020–2333 UTC 9 Mar (RF23)		2209–0107 UTC 4 Feb (RF11)		0108–0420 UTC 16 Mar (RF24)		1442–1807 UTC 17 Feb (RF17)	
		Obs	WRF	Obs	WRF	Obs	WRF	Obs	WRF
No. of flight legs composited	_	9		12		11		11	
Low-level ^a BV frequency N	10^{-3} s^{-1}	8.5	6.0	7.0	6.7	9.0	7.9	2.2	2.9
Froude number Fr ^b	_	0.46	0.73	0.41	0.81	0.45	0.66	4.5	3.4
Peak deep updraft ^c	$\mathrm{m}\;\mathrm{s}^{-1}$	0.48	1.23	0.57	1.57	0.63	0.73	1.22	1.56
Peak flight-level LWC	$\rm g~kg^{-1}$	0.02	0.11	0.06	0.09	0.08	0.51	0.23	0.13
Max orographic enhancement ^d	_	1.6	3.0	2.3	1.8	1.8	1.9	2.0	_

^a Between the surface at Crouch and 2.5 km above MSL, the approximate crest height of the Idaho Central Mountains.

The model overestimates the wave amplitude by a factor of ~ 2 (Fig. 6, Table 1). This may be due to an underestimation of the low-level stability in the Payette basin and, thus, an overestimation of the Froude number (Table 1); in other words, the modeled low-level flow is coupled better to the underlying terrain.

Linear theory (the Taylor-Goldstein equation) predicts that for 2D sinusoidal terrain with a wavelength λ , and no wind shear, gravity waves are vertically propagating (evanescent) when $\lambda > 2\pi(U/N)[\lambda < 2\pi(U/N)]$. Assuming $N = 10^{-2} \text{ s}^{-1}$ and $U = 10 \text{ m s}^{-1}$ at mountain crest level (Figs. 4a,d), the threshold spacing between ridges is a mere 6 km, less than the actual ridge spacing (\sim 10–25 km). This is consistent with the preponderant presence of deep waves, and an evanescent response evident only from the two sharpest crests. We believe these deep waves have characteristics of vertically propagating waves, given that amplitude is maintained with height, and given positive w' and negative $u^{*'}$ perturbations on the upwind side of the crests (and the reverse in the lee) (Figs. 4g,j), as predicted by linear theory (Durran 2003). Such waves normally tilt upstream, as they propagate energy upward. The observed waves do not appear to tilt much, although note the transects' height exaggeration, by a factor of 5.7. The Scorer parameter ℓ^2 decreases with height in the valley, to near zero values at 2.0 km AGL (the level of the mountain tops surrounding Crouch), and stays very low at higher levels (Fig. 4b), indicating no singular wave trapping level aloft. The model captures similar N and ℓ^2 profiles, except at very low levels in the Payette River basin around Crouch (Fig. 1b), where the model does not capture the cold pooling.

The along-track wind is denoted as u^* . For track A, u^* equals the zonal wind u. The anomaly $u^{*\prime}$ is computed by subtracting the height-dependent average, $u^{*\prime} = u^* - \overline{u^*}(z)$, for the composite cross section, for both WCR and WRF data. The $u^{*\prime}$ transect only reveals minor wavelike patterns (Fig. 4j) in support of the observed terrain-driven vertical drafts as expected from linear theory. Ridge 5 displays the best crest-level convergence on its upstream side (consistent with linear theory), and divergence to the right, near the crest itself. The

primary along-track (zonal) pattern is low-level (2–4 km MSL) convergence and net divergence higher up (4–7 km MSL), part of a mesoscale wave triggered by the Idaho Central Mountains (Fig. 1a). The model wind anomaly pattern is broadly consistent: it captures the same basic pattern, as well as the shallow dipole structure around ridge 5.

What explains this basic cross-mountain wind pattern? A key factor is that over the distance of track A (95 km), the average terrain height increases from west to east (a mean slope of 1.1% or 11 m km $^{-1}$). The derivation of the WCR w'field assumes that the track-mean $\overline{w} = 0$ (section 2b), yet the observed cross-mountain convergence now brings this assumption into question. Ignoring cross-track (meridional) convergence, air density variations, and any vertical motion at ground level, vertical integration of the WCR-observed along-track convergence between 1.5 and 4 km MSL yields a track-mean updraft \overline{w} increasing to 0.15 m s⁻¹ at 4.0 km, and then decreasing higher up, up to the highest data level (flight level) (Fig. 7). The model, without such simplifying assumptions, also produces a track-average updraft, although weaker (up to 0.10 m s^{-1}) and shallower (peaking at 1.9 km MSL). This indicates that the O(100) km ascent is driven, to a first order, by mesoscale cross-mountain convergence. In summary, there is a track-mean updraft \overline{w} , consistent with the mean terrain slope from west to east along track A. A lowlevel along-track wind of 10 m s⁻¹ (Figs. 4d,i,n) impinging on such slope produces an average updraft of 0.11 m s⁻¹ (Fig. 7). The weaker model \overline{w} value implies that there is some compensating along-mountain divergence, especially between 2 and 3 km MSL, as confirmed by model output: The vertical velocity derived from the model cross-mountain convergence exceeds the model \overline{w} and is close to the WCR-derived value (Fig. 7). The three other cases discussed below reveal a similar pattern of low-level convergence and midlevel divergence, and similar model \overline{w} profiles, in shape and magnitude, between the surface and cloud top (Fig. 6).

Armed with this information, we could revise the WCR \overline{w} assumption ($\overline{w} = 0$), to account for the terrain-induced average updraft (section 2b). The model \overline{w} profile shown in Fig. 7

^b Fr is defined as Fr = $\overline{U}/(\overline{N}H)$, where \overline{U} and \overline{N} are calculated over a depth H=1570 m, from the surface at Crouch to 2.5 km MSL.

^c Column-average w' between 2.6 < z < 6.0 km, i.e., above the terrain (and the melting-layer contamination) and up to the upper level with continuous WCR data.

^d Defined as the ratio of the maximum precipitation rate to the leg-average precipitation rate. In RF17, the model precipitation was too light and local for this calculation. The observed precipitation rate is estimated from the WCR, after correction for attenuation.

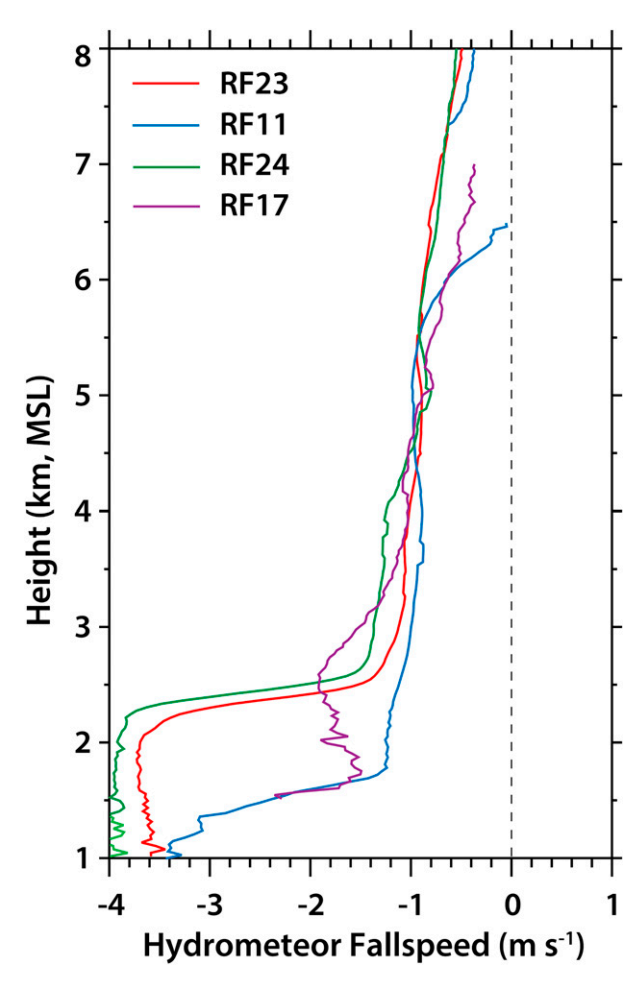


FIG. 5. Track-average hydrometeor fall speed $\overline{V_T}$ for each composite research flight estimated from the WCR zenith and nadir beams.

contains not just the 100-km-scale topographic forcing, but also the synoptic-scale component (typically 1–10 cm s⁻¹) responsible for the deep stratiform precipitation system (Fig. 3a). The model \overline{w} is small compared to the amplitude of the gravity wave (Figs. 4g, 6), so we chose not to revise our best-estimate air vertical motion field. Nevertheless, this mesoscale \overline{w} is important in understanding cloud microphysical processes across the larger-scale terrain within the cross section, as discussed below.

b. Track A: Research flight 23: Cloud and precipitation response

No 2D observations of LWC exist, but we do have flight-level LWC measurements. The flight levels range between 3.4 and 7.2 km MSL in RF23 (marked with unit length ticks on the left side of Fig. 4g). Time- and space-matched model data are compared to flight-level data in Fig. 8: for each UWKA longitude bin at a given height, an inverse distance interpolation is used, with the nearest four model grid points in the vertical (z) and horizontal (x) directions. Given that the flight

levels are relatively high and vary over almost 4 km, and that the LWC is near zero at the higher levels, both in observations and in the model, the averages are rather small. The WRF Model has flight-level-average maxima in LWC of 0.05-0.1 g kg⁻¹, located near the downwind end of the main wave updrafts (Fig. 8a), as expected (e.g., Fig. 2 in Wang et al. 2012): In a mixed-phase cloud, the LWC is related to the time-integrated excess condensation (due to the vertical displacement) over LW consumption by snow. The observed LWC is similarly modulated by wave updrafts (Fig. 8a), but because these updrafts are weaker than in the model, less LW is observed (the flight-level average peaks at just 0.02 g kg⁻¹, Table 1). More specifically, flight-level observations suggest that the model exaggerates the updrafts between peak 4 and 5 as well as upstream of peak 6 (Fig. 8a). These are also regions where the model overproduces LWC.

The WRF Model produces much higher LWC maxima below the lowest flight level, up to 0.4 g kg⁻¹ near every ridge, or more specifically, toward the downwind end of every updraft (Figs. 4k,l). This simulated liquid consists of cloud water and also melted snow (rain) below the freezing level (~2.4 km).

The model equivalent reflectivity (shown in Fig. 4m) is computed using assumptions in the Reisner-2 scheme of MM5 (Reisner et al. 1998). That scheme assumes Rayleigh scattering only, similar to an S-band radar, and no path-integrated attenuation or other range-dependent effects. The WCR (W-band) reflectivity (Fig. 4h) is much lower on account of Mie scattering, saturating around 15–20 dBZ, and may be impacted by attenuation (section 2b). Here, we examine spatial patterns only, we do not compare model versus observed reflectivity values.

Remarkably, the WCR reflectivity shows no wave pattern in sync with the vertical velocity pattern (Fig. 4h). A distinct reflectivity maximum is present only over, or rather just downwind of, the main ridge (5). This suggests that the residence time of hydrometeors (snow) in a gravity wave updraft (~3–6 min) generally is small compared to the time scale of snow growth/sublimation, i.e., the size distribution changes little across the waves and varies more with height. The relative humidity is depressed, especially behind ridge 5 (Fig. 4o). Even near the cloud top, reflectivity is not visibly modulated by the gravity waves, in this or the three other cases with deep stratiform precipitation discussed below.

The combination of hydrometeor vertical velocity w_H and along-track wind u^* yields the instantaneous hydrometeor trajectories (i.e., hydrometeor streamlines). Such trajectories (illustrated in Figs. 4f,i) are directly radar measured: the only assumption is steady-state flow, which applies, given that these are time-averaged (composite) velocities. Note that w_H is reflectivity weighted (by the nature of Doppler measurements); thus, the trajectories apply specifically to the largest hydrometeors. These hydrometeor trajectories are rather flat aloft, steepening as they approach the ground, due to a wind speed decrease and a V_t increase, especially across the melting layer. The trajectories show only minor vertical deformations in the gravity wave flow field, as was observed also by Heimes et al. (2022). Virtually no particle ascent occurs: at best, hydrometeor paths are nearly level, in places where w_H approaches

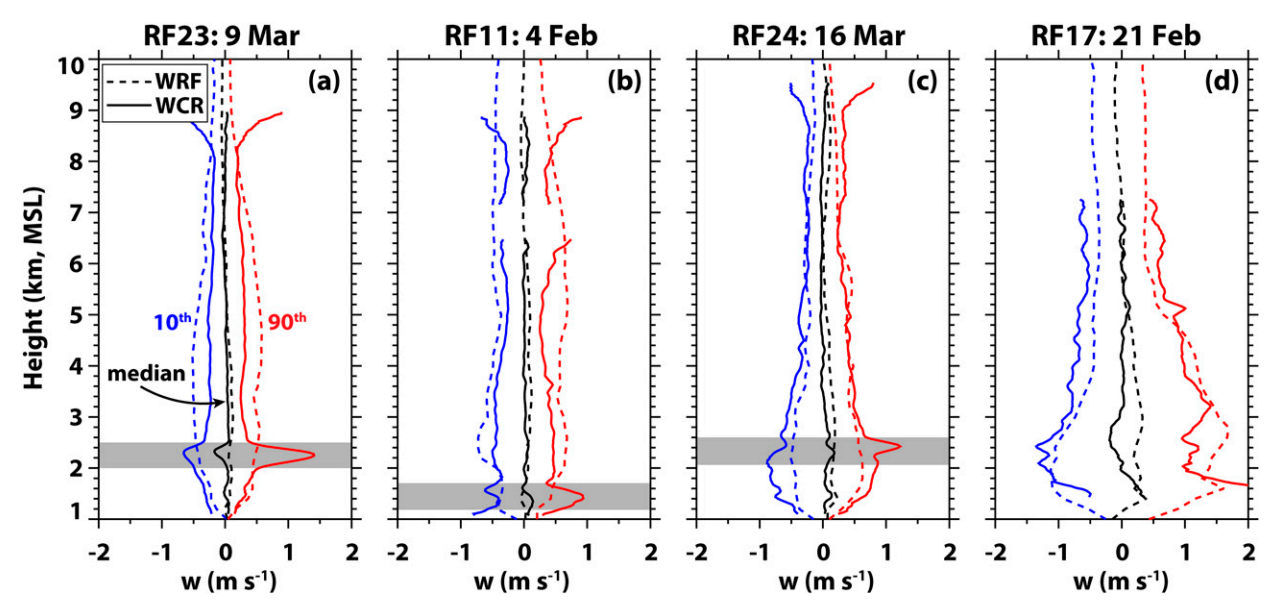


FIG. 6. Frequency by altitude distribution of air vertical velocity for (a) 9 Mar 2017, during RF23; (b) 4 Feb, during RF11; (c) 16 Mar, during RF24; (d) 17 Feb, during RF17. Shown are the 10th, 50th (median), and 90th percentiles. Solid lines refer to WCR observations w'; dashed lines refer to time–space-matched WRF Model output w. WCR levels with fewer than 200 points are excluded. WCR data are contaminated by a sloping freezing level in the gray belts.

zero (Fig. 4f). The successive ridges are close enough that most ice crystals, starting near cloud top, experience multiple gravity wave ascents and descents before reaching the ground. That is, any effect of these mid- to upper-level vertical motion perturbations on precipitation is felt over the downwind ridges, not locally.

Low-level reflectivity increases from left to right, consistent with the low-level ascent of the westerly current from the Snake River basin to the Central Mountains. The WRF Model reflectivity pattern (Fig. 4m) generally is consistent with the WCR reflectivity pattern (Fig. 4h). Individual ridges do produce low-level maxima in the mixing ratios of cloud liquid water and graupel (both up to 0.4 g kg⁻¹) (Fig. 4k), but the mixing ratio of cloud ice + snow (which dominates reflectivity) shows little modulation by the gravity wave vertical drafts (Fig. 4k). The same applies at flight level, especially in observations, but also in the WRF simulations (Fig. 8a). Interestingly, a few maxima in the graupel mixing ratio (Fig. 4k) (which explain the corresponding maxima in model reflectivity, Fig. 4m) are present in the low-level shear zone (2.0–2.5 km MSL) over the high terrain to the east, possibly due to modelresolved² overturning cells (Houze and Medina 2005), or due to the recirculation of liquid drops through the melting layer (Korolev et al. 2020). Because these are time-averaged fields, either process must be impacted by the underlying terrain. Similar reflectivity maxima are present, but less apparent, in the WCR observations (Fig. 4h).

The rather insignificant response of cloud ice and snow to a ridge–valley terrain pattern, and stronger enhancements in cloud liquid water, have been described in stratified warm sectors upstream of the Olympic Mountains also (Fig. 11 in Zagrodnik et al. 2021). In isolated lenticular clouds, ice may be initiated in the wave updrafts as a result of high supersaturation values, resulting in a dramatic increase in radar reflectivity near the wave crest (Wang et al. 2012). This is not observed here, presumably because ice is present already upstream in these deep clouds, and the wave amplitude is relatively small compared to the example in Wang et al. (2012).

Along-track model precipitation (Fig. 9a) is highly correlated with terrain elevation and the orographic gravity waves (Fig. 41), at least for the major ridges (4, 5, and 6). In general, higher terrain receives greater precipitation, except for the easternmost ridge. More specifically, the maxima of model precipitation are located in the lee of mountain peaks, within the gravity wave downdrafts. So, while model updrafts enhance LWC and growth by riming on the upwind side (Fig. 4k), the peak in surface precipitation is displaced just downwind of these rather narrow ridges. The downwind displacement of the precipitation maximum could have been larger, given the hydrometeor trajectories (Fig. 4f), but the enhanced LWC and snow/ graupel/rain growth are very shallow (Fig. 4k). There is a secondary precipitation maximum in the valley between ridges 4 and 5 (Fig. 9a). This maximum is associated with (just downwind of) the lee-wave updraft mentioned before.

WCR reflectivity (Z, mm⁶ m⁻³) is converted to snowfall rate (S, mm h⁻¹) using an empirical W-band Z–S relation developed from data collected over mountains in the interior western United States by Pokharel and Vali (2011), i.e., $S = 0.39Z^{0.58}$, which they found was valid between -25 and

² At 900 m grid resolution, instantaneous model output reveals a few transient updraft-downdraft couplets near mountain crest level, but mostly resembles the composite field shown in Fig. 4l, without breaking Kelvin-Helmholtz billows as observed by WCR in a similar environment (Grasmick and Geerts 2020).

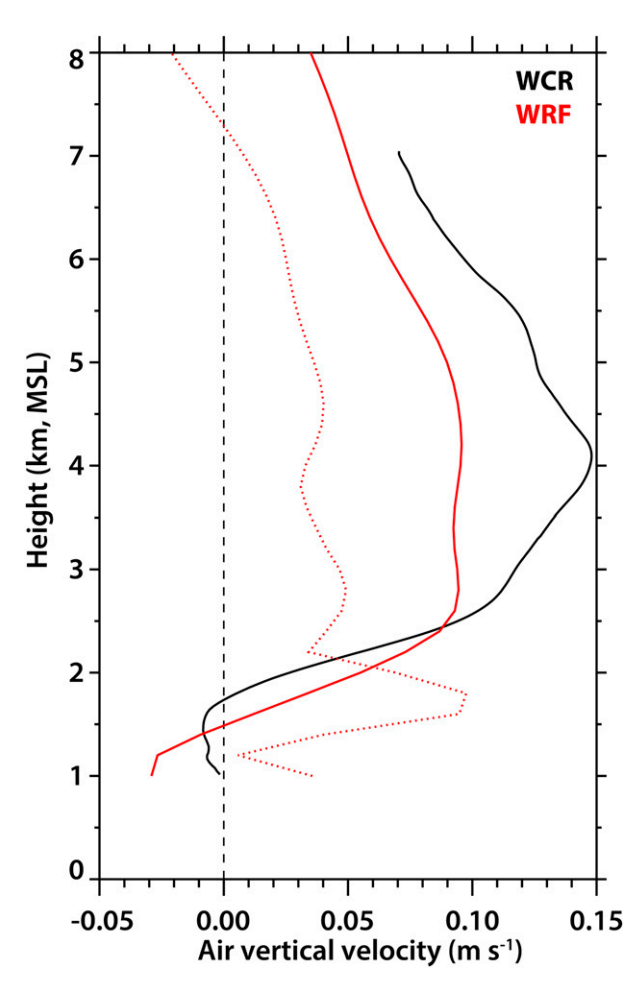


FIG. 7. Average air vertical velocity profiles along track A during RF23 estimated from vertically integrated 1D convergence using WCR dual-Doppler data (black) and matching WRF along-track wind data (solid red). Also shown is the actual track-average \overline{w} from WRF (dotted red).

15 dBZ. Here, Z is measured just above the melting level (2.5 km MSL in RF23), so as to avoid brightband contamination (Fig. 9a). W-band reflectivity is attenuated by liquid water; a correction³ for this path-integrated attenuation assuming model LWC (shown in Fig. 4k) gives the red line in Fig. 9a. We assume this to be the best-guess radar-derived precipitation rate. This rate shows some similarities with modeled surface precipitation rate, with the highest values associated with the three main updrafts (the lee-wave updraft in the Middle Fork Payette River valley, and those at ridges 5 and 6, Fig. 9a). Also consistent with the model, the WCR-derived precipitation rate shows little or no sensitivity to the local terrain ridges 1–3.

But there are important differences: Whereas the simulated orographic precipitation enhancement rate is a factor of 3

(Table 1), the radar-derived spatial variation in precipitation rate is much smaller (Fig. 9a). The model may overestimate the terrain-driven precipitation modulation, because it appears to overestimate LWC (Fig. 8a). On the other hand, the radar observations may underestimate this modulation, because *hydrometeor sorting* may occur, i.e., the selective fallout of graupel (high *S* for a given *Z*) ahead of low-density snow (with high *Z* but small contribution to *S*) on the lee side. A single *Z*–*S* relationship does not account for hydrometeor distribution variations along the track. Another cause for the disagreement is that the model precipitation is evaluated at the surface, and the WCR-based precipitation is evaluated just above the melting layer, which was rather high for RF23.

c. Track A: Research flight 11

The characteristics of stratified flow over terrain, including gravity waves, wave trapping and wave breaking, are highly dependent on upstream stability and cross-mountain wind profiles (e.g., Durran 2003). To examine how robust the findings for RF23 are for other winter storms, we examine RF11, a case with similar stability and wind properties as RF23.

The synoptic weather pattern during RF11 (2300 UTC 4 February 2017) was similar to that during RF23: An upperlevel trough off the west coast, a mostly zonal jet along a broad upper-level ridge over the SNOWIE domain (Fig. 2c), and a frontal boundary just north of the zonal transect of interest (Fig. 2d). The transect from the coast to NW Wyoming again displays a moist air mass (Fig. 3b) with wind speeds similar to those in RF23, although the integrated vapor transport (not shown) is lower in RF11 than in RF23, because the air mass is colder and the moist plume shallower (Fig. 3). A wellmixed moist layer, 3-4 km deep, is advected inland, capped by a stable dry layer whose base rises in height from ~4 km MSL along the west coast to ~6 km MSL in the SNOWIE domain (Fig. 3b). An upper-level moist layer is present just below the tropopause (Fig. 3b), evident as a cirrus layer in the SNOWIE region, separate from the lower cloud layer (Fig. 10h). The Crouch rawinsonde reveals a shallow layer of southerly flow, not as stable as during RF23 (Figs. 10a,e), but still blocked flow (Fr < 1, Table 1). Above this layer, westerly flow with little directional shear and weak stratification is present in the lower cloud layer (Fig. 10), all similar to RF23.

The RF11 vertical velocity composites (Figs. 10f,g) are remarkably similar to the RF23 composites (Fig. 4), in terms of the number, depth, and intensity of the deep updrafts (see also Fig. 6), including a lee-wave updraft between 4 and 5. The level with erroneous w' retrieval around the freezing level (Fig. 10g) again is due to a melting layer slightly tilting down toward the east. Both cases also witness the two shallow evanescent wave dipoles near the best-defined ridges (4 and 5). This can be attributed to the similarities in the profiles of crossmountain wind (Fig. 10d), stability (Fig. 10a), and Scorer parameter (Fig. 10b) in both cases. The WRF Model captures the stability and wind profiles very well (Figs. 10a-e). The model captures the spatial distribution of updrafts (Fig. 10l), although it again overestimates the strength of the vertical drafts, as in RF23 (Fig. 6, Table 1). The model and WCR data agree that

³ W-band two-way path-integrated attenuation by liquid is computed following Liebe et al. (1989).

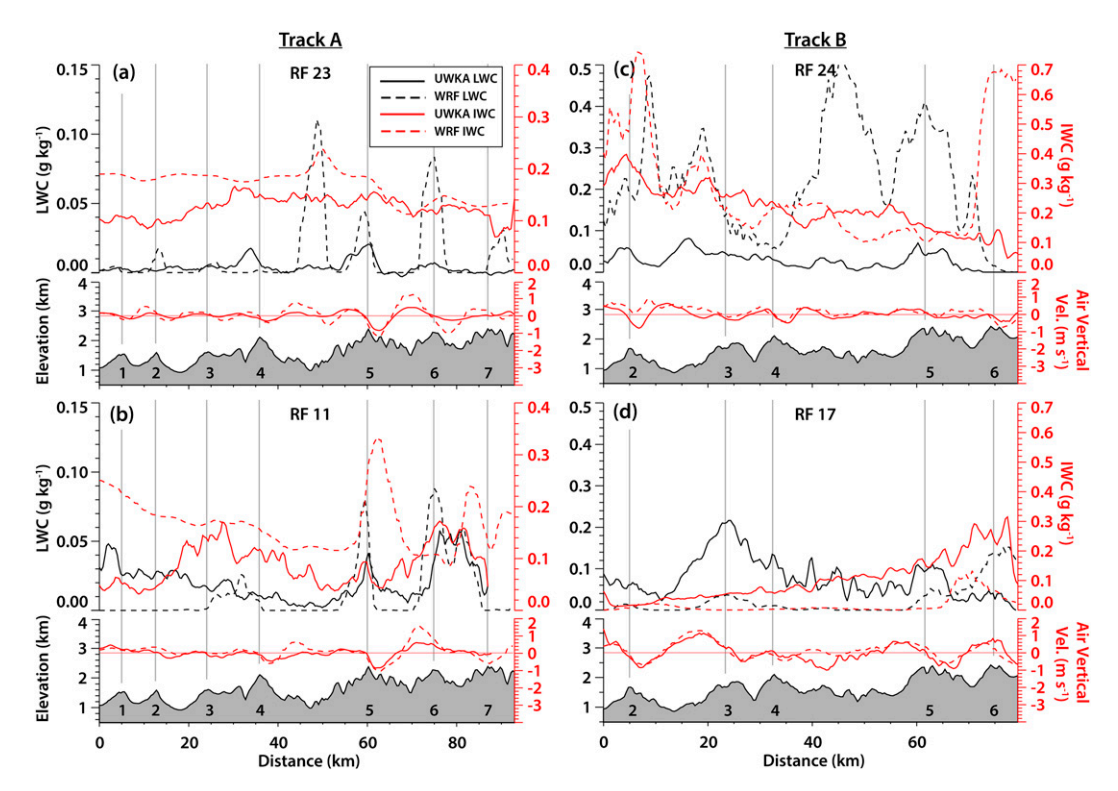


FIG. 8. Composite flight-level LWC (black) and IWC (red) related to flight-level w' (red) and underlying terrain (black line with gray shading) for the same four cases as in Fig. 6. Solid lines refer to aircraft observations (Nevzorov for LWC and IWC, gust probe for w); dashed lines refer to time–space-matched WRF Model output. The flight-level distribution for each case is shown in Fig. 4g). The terrain ridges of interest are numbered along the lower horizontal axis, as in Fig. 1b.

above 4 and 5 km MSL, the updrafts are truncated or combined, resulting in just three main wave updrafts aloft in RF11.

As in RF23, the boundary layer slopes upward toward the east (Fig. 10i). Therefore, the u' and convergence patterns are basically the same as in RF23. The WCR-derived hydrometeor trajectories, some of which are shown in Figs. 10f and 10i, are also very similar to the ones for RF23. The cloud and precipitation response in RF11 is similar as well: the WCR reflectivity field (Fig. 10h) aloft shows no modulation by the gravity waves. It does reveal vestiges of shear-deformed, transient fall streaks between the ground and about 4 km MSL, streaks that are clear in individual transects (not shown). Generally, reflectivity increases from west to east at low levels. As in RF23, the model reflectivity does show some response to the terrain, with low-level maxima near or just downwind of the main ridges (4, 6, and especially 5). Model precipitation rates are highest at the same three locations (Fig. 9b). The WCRderived snowfall rate (Fig. 9b) again indicates weak terrainrelated variation, esp. near crest 6. Again, peaks in LWC at flight level are correlated with the strongest gravity wave updrafts (Fig. 8b). The modeled LWC is very close to the observed LWC on average in RF11, but the model LWC is more sensitive to the terrain. The model cross section (Fig. 101) reveals a much broader/deeper updraft upstream of ridges 5 and 6 than what was observed (Fig. 10g), explaining the high model LWC there (Fig. 8b).

RF11 only has a few minor differences, compared to RF23: It is a colder event (Fig. 10c) and, thus, has a lower freezing level (Fig. 10m), less liquid water and graupel (both up to 0.1 g kg^{-1}), and more snow (Fig. 10k). The echo-free zone around $\sim 6.7 \text{ km MSL}$ (Fig. 10h, and also in the WRF Model, Fig. 10m) is due to a dry wedge (Fig. 3b). Finally, there are slight differences in the w' field, as mentioned above, and the u^* wave response to the main peak (ridge 5) displays a slightly stronger deceleration (acceleration) on the west (east) side, both in observations (Fig. 10j) and in the model (Fig. 10o).

The remarkable similarities between RF23 and RF11 build confidence in the terrain-related conclusions reached for RF23. In fact, one can combine the two cases, i.e., all 21 WCR transects from RF23 + RF11, and all corresponding model transects and all sounding data, and produce a 15-panel figure similar to Figs. 4 and 10. Such a figure (not shown) is very similar to either Fig. 4 or Fig. 10. It highlights the impact of small-scale terrain features on a strong weakly stratified moist zonal current, and the impact of the flow perturbations on cloud microphysics and precipitation.

⁴ The discontinuity in WCR reflectivity in RF11 near x = 16 km (Fig. 10h) is due to fewer flight transects available in the composite for x < 16 km, and the available transects having lower low-level reflectivity.

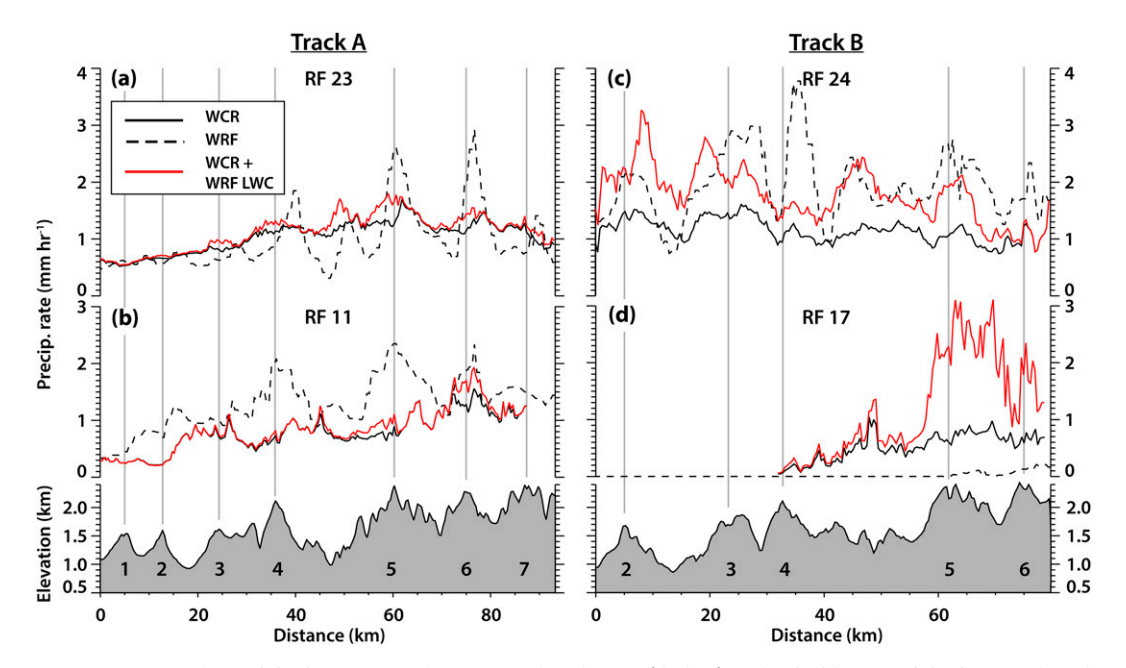


FIG. 9. WRF 3 h precipitation expressed as a mean hourly rate (dashed) and coincident precipitation rate based on the WCR composite reflectivity from just above the melting level (solid lines, using a Z–S relation) placed in the context of the underlying terrain for the same four cases. The black and red lines use the same Z–S relationship, but the red line results from Z values corrected for attenuation assuming model LWC (Fig. 9). The vertical lines highlight the terrain ridges of interest, which are numbered along the bottom horizontal axis, as in Fig. 1b.

d. Track B: Research flight 24

The terrain along track B is slightly different (Fig. 1b), with just 5 ridges that are somewhat more pronounced, less track perpendicular, and spaced farther apart than along track A. The far northeast (NE) end of track B is near the watershed divide between the Payette and Salmon River basins, whereas track A remains well east of this divide (Fig. 1b).

RF24 was flown in close proximity to a slow-moving Pacific cold front and a strong southwesterly jet aloft (Figs. 2e,f, 3c). A deep cold-frontal precipitation band (roughly aligned with the track) was present throughout the flight. The last two flight legs sampled shallow postfrontal clouds along the western end of the track. Moisture was advected from Northern California to the target area, along the transect that aligns with track B (Fig. 3c). Significant subsidence occurred in the lee of some upstream ranges along this transect at this time. For most RF24 transects, a deep well-mixed moist layer was present in the target area, as in RF23. Moist N values generally were below 10^{-2} s⁻¹ except at very low levels, in the Payette River basin near Crouch, where cold air pooled, again resulting in low-level blocked flow. Strong speed shear was present, but little directional wind shear, and no wave trapping layer (Figs. 11a-e, Table 1). This leads to a similar lowlevel convergence pattern (Fig. 11j) as along track A.

Again, the terrain produces a deep gravity wave response, but in this case the highest amplitude, deepest waves are found on the upstream side, one around ridge 2 (Squaw Butte) and a second over the valley just downstream of this ridge (Fig. 11g). The latter most likely is a resonant response

triggered by ridge 2 (trapped lee wave). The WRF Model captures these two strong wave updrafts (Fig. 111). Unlike the two previous cases, the model does not exaggerate the gravity wave amplitude in this case (Fig. 6c, Table 1).

RF24 is the warmest case (highest melting level, at \sim 2.5 km), and exceptionally high LWC values are simulated near the two lead updrafts and farther downwind of them at flight level (Fig. 8c), much more than observed (Table 1). The simulated LWC is especially high at midlevels, below \sim 4.3 km (Fig. 11k). It is no surprise, then, that these updrafts produce pockets of copious graupel in the model (Fig. 11k). In reality there is likely more cloud microphysical complexity than captured in the model. The Nevzorov LWC maxima line up well with the downstream end of the wave updrafts, but some observed pockets of LWC and IWC are associated with transient embedded convection in this case, especially near ridge 2.

Because of the strong wave updrafts on the upstream side of the transect, heavier precipitation occurs over the western foothills (compared to the high terrain to the east), according to both WCR observations and WRF simulations (Fig. 9c). Of all four cases examined here, RF24 has the highest radar reflectivity values (Fig. 9), the highest model snow and graupel mixing ratios (Figs. 8, 11k), and the heaviest precipitation rate (1.2 and 2.0 mm h⁻¹ on average, according to the attenuation-corrected WCR reflectivity and WRF, respectively). Precipitation is again modulated by the small-scale terrain, with maxima on the lee side of the individual ridges, but the relative difference between minima and maxima is smaller than in the other cases, implying little orographic enhancement (Table 1).

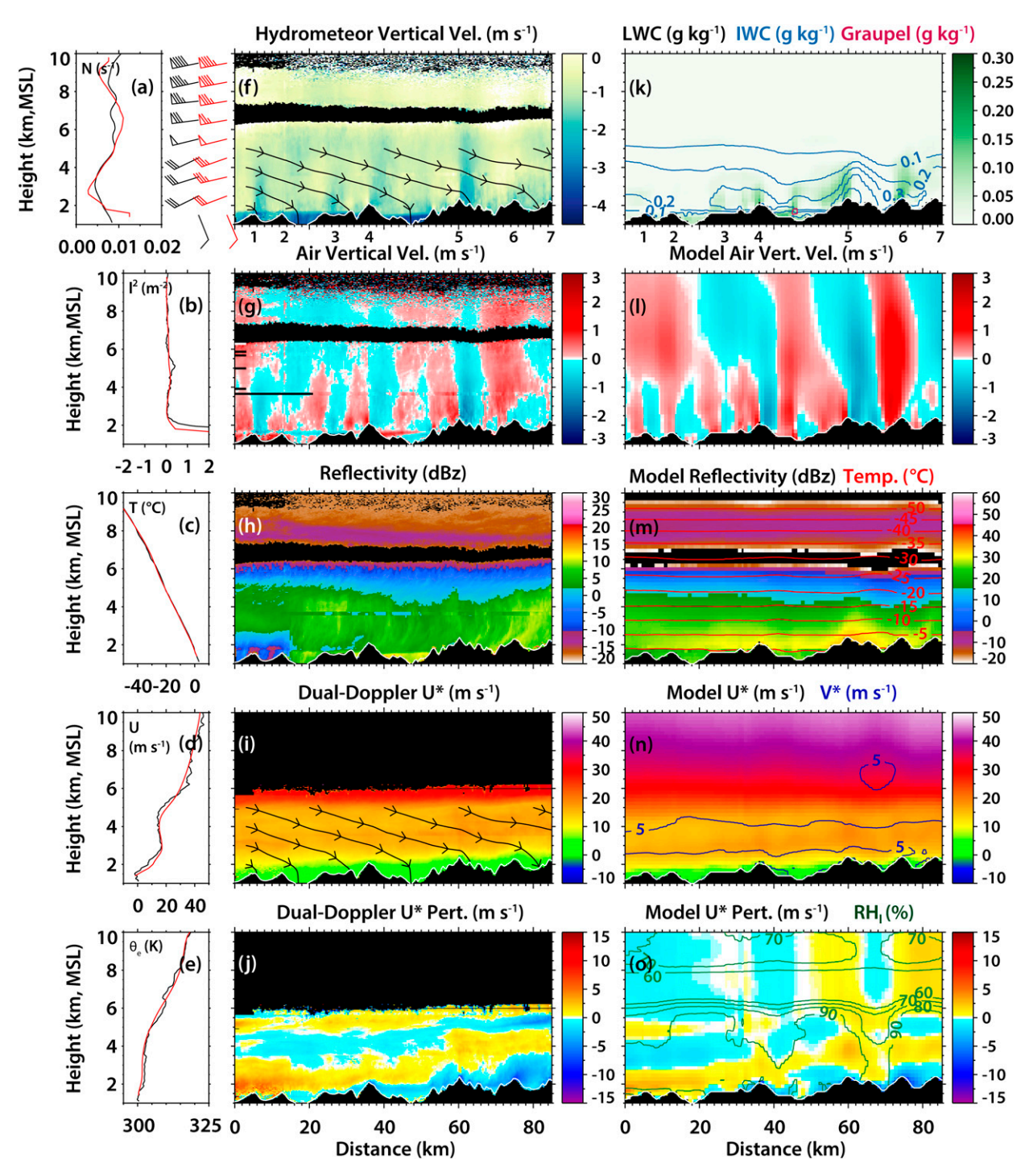


FIG. 10. As in Fig. 4, but for RF11 (4 Feb 2017).

(The WCR-based precipitation distribution estimation is less representative because Z values above the freezing level must be used, and the freezing level was quite high in RF24.) Strong subsidence is present in the lee of the watershed divide crest (6) (Figs. 11g,l), extending farther east than the transect width shown here, resulting in the evaporation

of cloud liquid water (Fig. 11k) and diminishing snowfall farther east.

e. Track B: Research flight 17

RF17 featured a significant synoptic change during the flight: a humidity gradient, associated with an occluded-frontal boundary

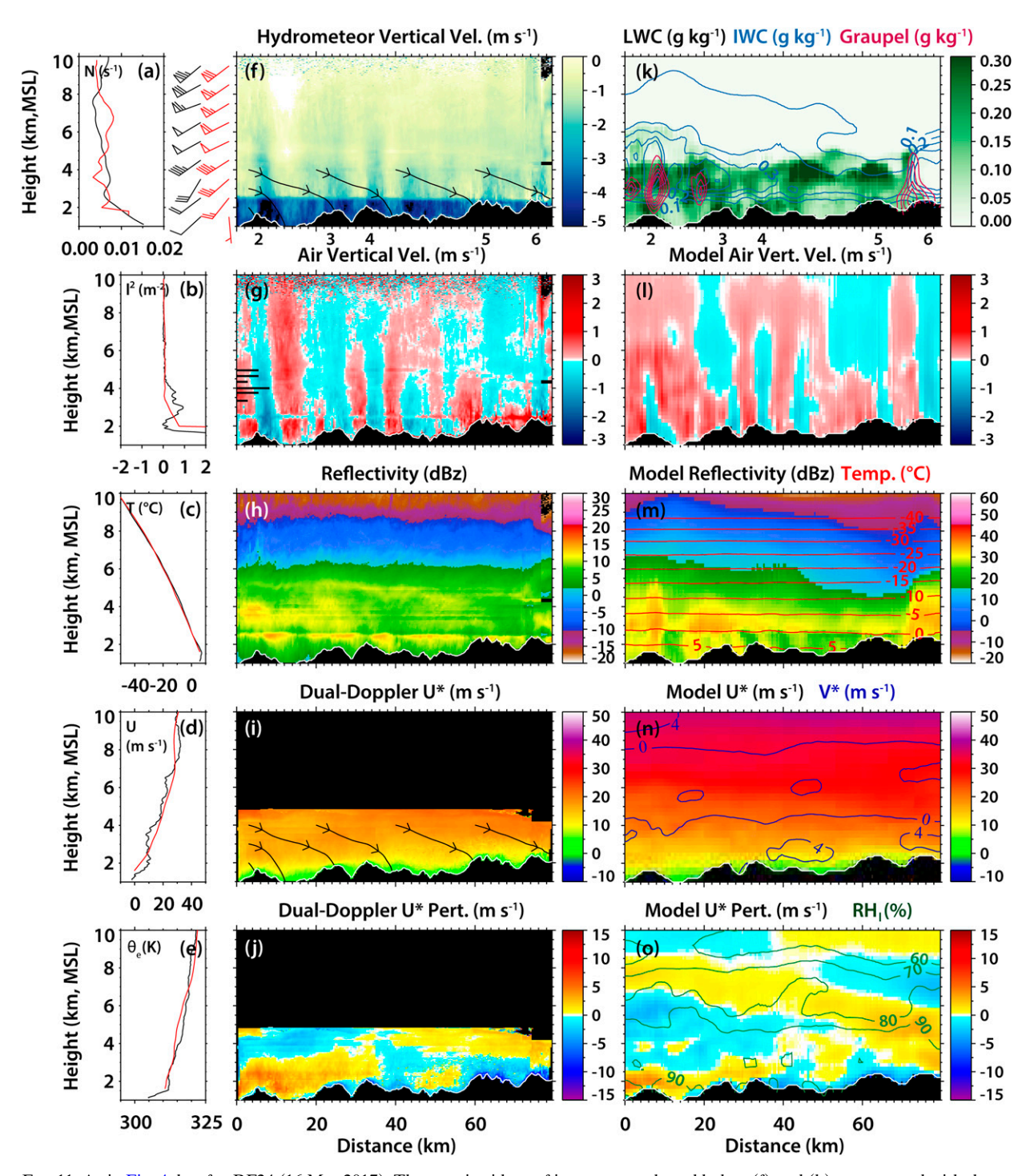


FIG. 11. As in Fig. 4, but for RF24 (16 Mar 2017). The terrain ridges of interest, numbered below (f) and (k), correspond with those in Fig. 1b.

roughly normal to the flight track (Figs. 2h, 3d), slowly moved to the NE during the UWKA flight. Frontal passage was associated not with cooling, but with drying at low to midlevels (Fig. 3d). During the last two flight legs, the UWKA sampled drier postfrontal conditions. The drying was associated with upper-tropospheric subsidence and a

low tropopause, part of an upper-level positive PV anomaly moving in behind a strong jet (Figs. 2g, 3d).

Unlike the three other cases, this case lacked low-level stability, in fact the θ_e contours in Fig. 3d indicate some potential instability at low levels (Fig. 12e). Therefore, the flow was unblocked (Fr \gg 1, Table 1). A well-mixed snowband enhanced

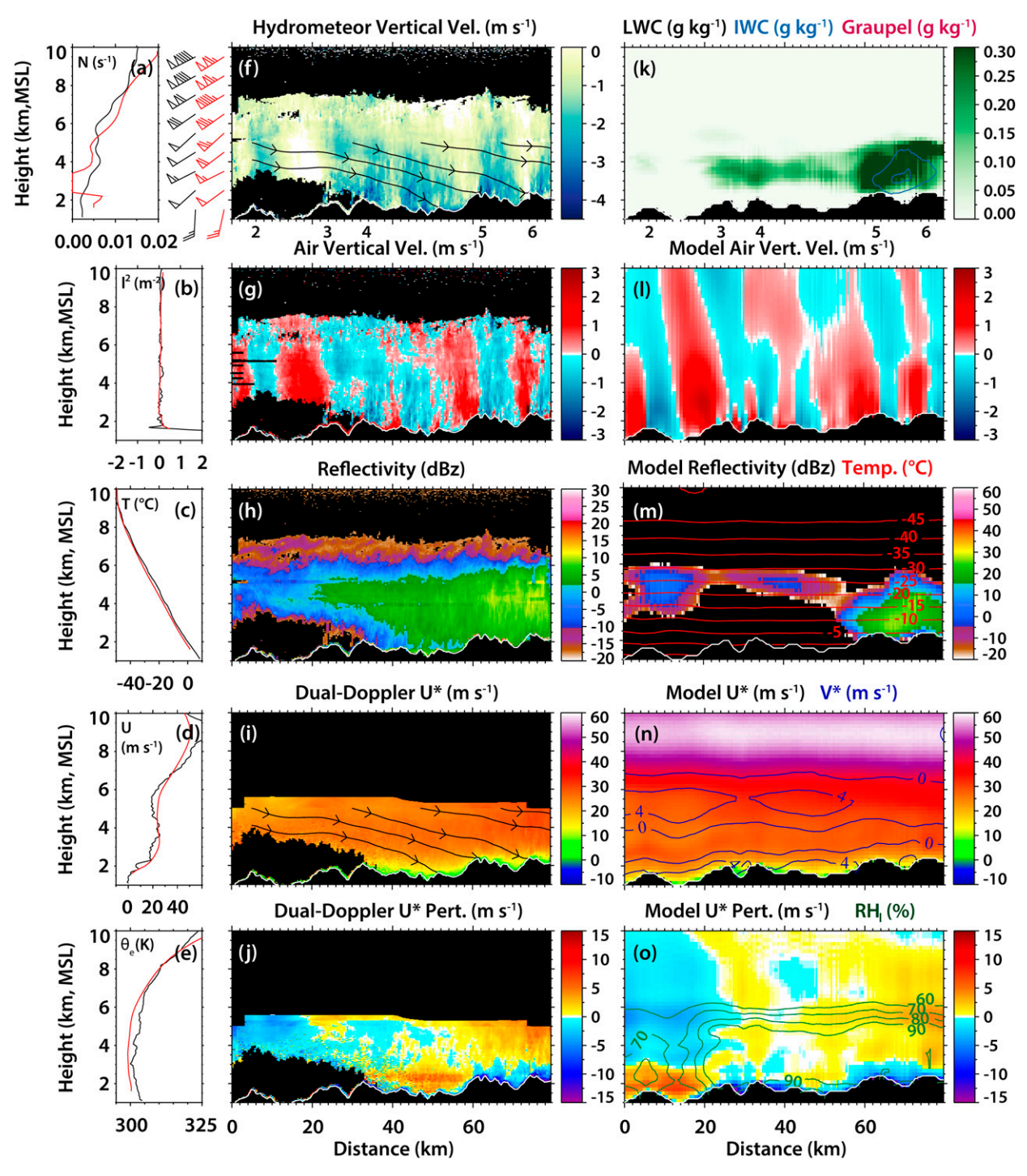


FIG. 12. As in Fig. 11, but for RF17 (21 Feb 2017).

by the terrain was sampled over the northeastern high terrain during all transects. Individual WCR transects also reveal some small embedded convective cells.

The Crouch rawinsonde data (and associated model output) (Fig. 12) reveal well-mixed conditions (low N values) up to cloud top near \sim 6 km MSL, and a veering wind profile with strong winds aloft. High-amplitude gravity waves are

present, both in the WCR and the WRF transects (Fig. 6d, Table 1), possibly on account of the strong winds aloft. The highest-amplitude waves are on the SW low-elevation side (Figs. 12g,l), as for RF24. The main wave updraft (the resonant updraft ahead of ridge 3) is strong enough to briefly lift snow particles (Fig. 12f), contributing to snowfall over the high terrain to the NW, before the snowband cleared out. The

intrusion of dry air from the SW (Fig. 120) eventually resulted in sublimation of snow falling from above the occluded front (Fig. 12h).

The model has the snowband a little too far to the east, and moves it out of the domain a little too early, with only a small amount of precipitation near the NE (right) end of the transect during the UWKA flight (Figs. 9d, 12m). Model correspondence is better if model output is shifted back in time, both by 1 and by 2 h (not shown). In the first flight hour, the model snowband contains rather high IWC (Figs. 8d, 12k), while in the remaining 3 h, generally high LWC values (some over 1.0 g kg⁻¹) remain over the eastern high ridges, with little ice and virtually no precipitation (not shown). The model has drier air moving in from the SW, mainly in the last hour (Fig. 12o). Time-matched composite model LWC, IWC, and precipitation values are lower than observed at flight level in this case (Figs. 8d, 9d), probably because of the premature midlevel dry air intrusion: The WCR indicates more midlevel ice particles on the upstream side than in the model (Fig. 12h). These particles are advected (Fig. 12i) into a region with high low-level LWC, resulting in heavy precipitation over the eastern high terrain, far heavier than in the model (Fig. 9d).

This model timing discrepancy aside, RF17 again shows clear modulation of vertical motion by the terrain: the strong wave updraft associated with ridge 3 (up to 1.5 and 1.7 m s⁻¹ at 4 km MSL according to the WCR and WRF, respectively) produces much flight-level LW before the dry air intrudes from the southwest (Fig. 8d). Both the WCR-derived snowfall rate (sampled at the lowest level, ~50 m above the terrain, because there is no melting layer in this case) and the model precipitation produce maxima just downwind of ridges 5 and 6 (Fig. 9d).

4. Discussion

As mentioned in the introduction, several studies have documented enhanced precipitation over rather small-scale terrain ridges in midlatitude mountain ranges, a process that seems to be captured rather well by sufficiently resolved WRF simulations. This study examines the connection between the atmospheric environment, orographic gravity wave structure, and microphysics/precipitation, using a sample of four cases along two different flight tracks. These cases do not represent a broad range of profiles of U, ℓ^2 , and N. The first three cases are similar, with low-level blocking and deep stratiform clouds. The fourth case, RF17, has unblocked flow and some weak embedded convection. The conditions sampled are rather typical for wintertime frontal disturbances, but other conditions (such as wave trapping or isolated postfrontal convection) are possible, and their cloud and precipitation response may be different.

Under the observed conditions, the WRF Model reproduces the observed vertical structure and spatial arrangement of the gravity waves over the terrain well: the stationary vertical velocity patterns are recurrent and reproducible by the model, both along track A (RF11 and RF23) and along track B (RF17 and RF24). The model tends to exaggerate the vertical velocity amplitude (Table 1) and, thus, the flight-level LWC

(Fig. 8, Table 1). The WRF simulations, at a grid resolution of 900 m, display a clear precipitation enhancement just downstream of the individual ridges (Fig. 9), especially the ridges with the strongest wave updrafts. The simulated maximum orographic precipitation enhancement (defined in Table 1) ranges between 1.8 and 3 for the cases examined here, and precipitation maxima tend to be found just *downwind* of the crests. In comparison, the orographic precipitation enhancement for the 800 m PRISM data along track A (B) is 1.7 (1.8), and the enhancement is slightly stronger on the *upwind* (westerly) side of the local terrain ridges (Fig. 1c). In follow-up work, a finer model grid resolution can be considered, fine enough to match the binned WCR data and to capture terrain-driven details such as evanescent waves.

The radar reflectivity field just above the freezing level (AFL) does vary somewhat in response to the wave updrafts, but because of a sloping melting level across the terrain in our cases, and significant precipitation growth at very low levels, the AFL radar reflectivity is a poor proxy for surface precipitation rate in these cases. Model output indicates that the wave-induced liquid water and graupel formation are shallow (Figs. 4k, 8k, 9k), and that orographic surface precipitation enhancement over small-scale ridges is due to processes very close to the ground.

Smith and Barstad (2004) present a linear analytical model for orographic precipitation with highly simplified cloud microphysics. The key parameters are wind speed U, stability N, mountain width, moist-layer depth, and two time scales, one for hydrometeor growth and one for hydrometeor fallout. Their assumed humidity profile is nearly saturated at all levels, allowing neglect of evaporation in valleys. This model is sufficient to capture the basic pattern of precipitation enhancement over small-scale terrain, e.g., on the west side of the Olympic Mountains (Smith and Barstad 2004) and in southern Norway (Barstad and Caroletti 2013). The present study details the processes involved in mixed-phase stratiform clouds: The deep gravity wave updrafts appear to have little impact on ice initiation and snow growth, at least in the cases examined here, but the high LWC at low levels near the downwind end of these updrafts does impact local precipitation, especially if the ridge is steep enough (and the impinging flow strong enough) for graupel growth and rapid fallout, mainly just downstream of the local ridge.

The exact location of the precipitation maximum, relative to the local terrain ridges, is likely to depend on the freezing level and precipitation type. The cases examined here generally had a low freezing level, with snow reaching the ground over the higher terrain. A higher freezing level implies a deeper layer of rain, with a higher fall speed than snow, thus moving the precipitation maximum in the upwind direction, toward the crest. Our cases involved stratiform ascent, and a rather rapid increase in reflectivity (or even a secondary reflectivity maximum, in RF24) in the -15° to -10°C region (Figs. 4h, 10h, 11h, 12h) (about 4.0-4.7 km MSL), most likely an indication of dendritic snow growth. The hydrometeor fall speed tends to increase in magnitude in this layer in all cases except RF11 (Fig. 5). Such acceleration contributes to moving surface precipitation in the upwind direction. The embedded

convection encountered in RF17 locally impacted updrafts, LWC, and IWC. Deep-convective ascent increases the moist-layer depth and may move the precipitation maximum farther downwind of the crest (Fuhrer and Schär 2005; Geerts et al. 2015). As the spacing between ridges increases well above the buoyancy wavelength, deeper lee descent is possible, drying out the lower atmosphere. In that case, slant hydrometeor trajectories are less likely to reach the next terrain updraft, except maybe for the highest ice particles, which may survive the descent and seed LW pockets forming over the next ridge (Reinking et al. 2000).

Further understanding of the systematic impact of local terrain on the flow, cloud and precipitation processes may be drawn from eddy-resolving simulations with a grid resolution at least 10 times finer than used in this study. Large-eddy simulations capture transient small-scale vertical velocity structures over complex terrain (e.g., Xue et al. 2022), so the isolation of terrain effects would require compositing, as was done here for the WCR transects.

5. Conclusions

This study uses airborne vertically profiling Doppler radar data plus output from a 900-m-grid-resolution WRF simulation with 81 vertical levels, to examine how relatively small-scale ridges (\sim 10–25 km apart and \sim 0.5–1.0 km above the surrounding valleys) impact the flow, cloud processes, and surface precipitation in deep stratiform precipitation systems. Two flight tracks are analyzed, each about 100 km long, between the Snake River plain and the Idaho Central Mountains. Data from \sim 10 repeat flight legs are composited for each of the four cases, in order to suppress transient flow and reflectivity features and retain the effect of the underlying terrain. The main conclusions are as follows:

- The local terrain ridges produce gravity waves that propagate vertically through the depth of the clouds. The horizontal and vertical structure of the up- and downdrafts is captured well by the WRF simulation. This was demonstrated already by Zaremba et al. (2022b). The wave amplitude is $\sim 0.5-1.2$ m s⁻¹ according to radar data, and \sim 0.7–1.6 m s⁻¹ in the model. The highest wave amplitude was observed in the case that lacked a low-level stable layer and produced embedded convective cells. Resonant lee waves and evanescent waves around sharp peaks are observed as well. While the analysis is 2D, 3D effects cannot be ignored. Over the full length of the transects examined here, between the upstream plains and the high terrain to the east, the upslope flow produces a track-average updraft, estimated at ~ 0.1 m s⁻¹ at low levels. This is consistent with the variation of the cross-mountain wind over this scale: mountain-scale low-level convergence and mid- to upper-level divergence are captured by both the radar and
- The gravity waves have no significant impact on radar or model-derived reflectivity in the deep stratiform cloud deck.

- The wind speeds aloft are high enough, the ridge spacing small enough, and the snowfall speed low enough that snow particles starting near cloud top encounter several gravity wave updrafts and downdrafts before reaching the ground.
- Liquid water is observed at flight level in wave updrafts, especially the stronger ones, peaking near the downwind end of these updrafts. These LWC peaks generally are more pronounced in the model, because of a slightly exaggerated simulated wave amplitude. Model and observations agree that in the cases examined here, the waves have little effect on IWC, except at very low levels where, according to the model, wave updrafts produce shallow pockets of high LWC and sometimes graupel.
- The model indicates substantial enhancement of surface precipitation just downwind of individual ridges, especially those with the most intense updrafts, with up to double to triple the average. The downwind displacement is small, because simulated precipitation enhancement over small-scale ridges is due to processes close to the ground, too low for in situ aircraft observations. Precipitation rate estimation with a profiling airborne radar is complicated by the melting layer. WCR reflectivity, sampled at the lowest meaningful level (just above the melting level), shows less modulation by the terrain. This may be due to hydrometeor sorting, in which case a single Z–S relationship is not representative.

Acknowledgments. We are grateful to Dalton Behringer for the manually corrected Nevzorov IWC. The Idaho Power Company (IPC) launched the rawinsondes from Crouch. This paper benefitted from comments by James Steenburgh and James Doyle. This study was funded by the National Science Foundation Grants AGS-1547101, AGS-1546963, AGS-1546939, AGS-2016106, AGS-2015829, and AGS-2016077. Funding for the deployment of the UWKA and WCR in SNOWIE was funded by AGS-1441831.

Data availability statement. Data collected during the SNOWIE Campaign are available to the public from the Earth Observing Laboratory data archive hosted by the National Center for Atmospheric Research. Flight-level aircraft measurements can be retrieved from https://doi.org/10.15786/M2MW9F (University of Wyoming Research Flight Center 2017a) and WCR data can be retrieved from https://doi.org/10.15786/M2CD4J (University of Wyoming Research Flight Center 2017b). The processed Nevzorov LWC and IWC content data are described in French and Behringer (2021).

REFERENCES

Barstad, I., and G. N. Caroletti, 2013: Orographic precipitation across an island in southern Norway: Model evaluation of time-step precipitation. *Quart. J. Roy. Meteor. Soc.*, 139, 1555–1565, https://doi.org/10.1002/qj.2067.

Cann, M. D., K. Friedrich, J. R. French, and D. Behringer 2022: A case study of cloud-top Kelvin–Helmholtz waves near the

- dendritic growth zone. *J. Atmos. Sci.*, **79**, 531–549, https://doi.org/10.1175/JAS-D-21-0106.1.
- Chu, X., B. Geerts, L. Xue, and R. Rasmussen, 2017: Large-eddy simulations of the impact of ground-based glaciogenic seeding on shallow orographic convection: A case study. J. Appl. Meteor. Climatol., 56, 69–84, https://doi.org/10.1175/JAMC-D-16-0191.1.
- Crook, N. A., 1988: Trapping of low-level internal gravity waves. J. Atmos. Sci., 45, 1533–1541, https://doi.org/10.1175/1520-0469(1988)045<1533:TOLLIG>2.0.CO;2.
- Daly, C., M. Halbleib, J. I. Smith, W. P. Gibson, M. K. Doggett, G. H. Taylor, J. Curtis, and P. P. Pasteris, 2008: Physiographically sensitive mapping of climatological temperature and precipitation across the conterminous United States. *Int. J. Climatol.*, 28, 2031–2064, https://doi.org/10.1002/joc.1688.
- Damiani, R., and S. Haimov, 2006: A high-resolution dual-Doppler technique for fixed multiantenna airborne radar. *IEEE Trans. Geosci. Remote Sens.*, 44, 3475–3489, https://doi.org/10.1109/ TGRS.2006.881745.
- Douglas, C. K. M., and J. Glasspoole, 1947: Meteorological conditions in heavy orographic rainfall in the British Isles. *Quart. J. Roy. Meteor. Soc.*, 73, 11–42, https://doi.org/10.1002/qj. 49707331503.
- Durran, D., 2003: Lee waves and mountain waves. *Encyclopedia of Atmospheric Science*, Elsevier Science, 1161–1170.
- French, J. R., and D. Behringer, 2021: UW King Air manually corrected Nevzorov Liquid/total/ice water content, version 1.0. UCAR/NCAR Earth Observing Laboratory, accessed 10 June 2021, https://doi.org/10.26023/2QRK-XSBA-RS0P.
- —, S. J. Haimov, L. D. Oolman, V. Grubišić, S. Serafin, and L. Strauss, 2015: Wave-induced boundary-layer separation in the lee of the Medicine Bow Mountains. Part I: Observations. *J. Atmos. Sci.*, 72, 4845–4863, https://doi.org/10.1175/JAS-D-14-0376.1.
- Fuhrer, O., and C. Schär, 2005: Embedded cellular convection in moist flow past topography. J. Atmos. Sci., 62, 2810–2828, https://doi.org/10.1175/JAS3512.1.
- Garreaud, R., M. Falvey, and A. Montecinos, 2016: Orographic precipitation in coastal southern Chile: Mean distribution, temporal variability, and linear contribution. *J. Hydrometeor.*, 17, 1185–1202, https://doi.org/10.1175/JHM-D-15-0170.1.
- Garvert, M. F., B. Smull, and C. Mass, 2007: Multiscale mountain waves influencing a major orographic precipitation event. *J. Atmos. Sci.*, **64**, 711–737, https://doi.org/10.1175/JAS3876.1.
- Geerts, B., and Q. Miao, 2005: The use of millimeter Doppler radar echoes to estimate vertical air velocities in the fairweather convective boundary layer. J. Atmos. Oceanic Technol., 22, 225–246, https://doi.org/10.1175/JTECH1699.1.
- —, Y. Yang, R. Rasmussen, S. Haimov, and B. Pokharel, 2015: Snow growth and transport patterns in orographic storms as estimated from airborne vertical-plane dual-Doppler radar data. *Mon. Wea. Rev.*, **143**, 644–665, https://doi.org/10.1175/ MWR-D-14-00199.1.
- Grasmick, C., and B. Geerts, 2020: Detailed dual-Doppler structure of Kelvin–Helmholtz waves from an airborne profiling radar over complex terrain. Part I: Dynamic structure. *J. Atmos. Sci.*, 77, 1761–1782, https://doi.org/10.1175/JAS-D-19-0108.1.
- Heimes, K., and Coauthors, 2021: Vertical motions in orographic cloud systems over the Payette River basin. Part III: An evaluation of the impact of transient updrafts on targeting during orographic cloud seeding operations. *J. Appl. Meteor. Climatol.*, 61, 1753–1777, https://doi.org/10.1175/JAMC-D-21-0230.1.

- Houze, R. A., Jr., and S. Medina, 2005: Turbulence as a mechanism for orographic precipitation enhancement. *J. Atmos. Sci.*, 62, 3599–3623, https://doi.org/10.1175/JAS3555.1.
- Ikeda, K., and Coauthors, 2010: Simulation of seasonal snowfall over Colorado. Atmos. Res., 97, 462–477, https://doi.org/10. 1016/j.atmosres.2010.04.010.
- Jing, X., B. Geerts, Y. Wang, and C. Liu, 2017: Evaluating seasonal orographic precipitation in the interior western United States using gauge data, gridded precipitation estimates, and a regional climate simulation. *J. Hydrometeor.*, 18, 2541–2558, https://doi.org/10.1175/JHM-D-17-0056.1.
- Kingsmill, D. E., P. O. G. Persson, S. Haimov, and M. D. Shupe, 2016: Mountain waves and orographic precipitation in a northern Colorado winter storm. *Quart. J. Roy. Meteor. Soc.*, 142, 836–853, https://doi.org/10.1002/qj.2685.
- Kirshbaum, D. J., and D. R. Durran, 2004: Factors governing cellular convection in orographic precipitation. *J. Atmos. Sci.*, 61, 682–698, https://doi.org/10.1175/1520-0469(2004)061<0682: FGCCIO>2.0.CO:2.
- Korolev, A., J. W. Strapp, G. A. Isaac, and E. Emery, 2013: Improved airborne hot-wire measurements of ice water content in clouds. *J. Atmos. Oceanic Technol.*, 30, 2121–2131, https://doi.org/10.1175/JTECH-D-13-00007.1.
- —, and Coauthors, 2020: A new look at the environmental conditions favorable to secondary ice production. *Atmos. Chem. Phys.*, 20, 1391–1429, https://doi.org/10.5194/acp-20-1391-2020.
- Lenschow, D. H., 1972: The measurement of air velocity and temperature using the NCAR Buffalo aircraft measuring system. NCAR Tech. Note NCAR-TN EDD-74, 39 pp., https://doi.org/10.5065/D6C8277W.
- Liebe, H. J., T. Manabe, and G. A. Hufford, 1989: Millimeter-wave attenuation and delay rates due to fog/cloud conditions. IEEE Trans. Antennas Propag., 37, 1617–1612, https://doi.org/10.1109/8.45106.
- Lundquist, J., M. Hughes, E. Gutmann, and S. Kapnick, 2019: Our skill in modeling mountain rain and snow is bypassing the skill of our observational networks. *Bull. Amer. Meteor. Soc.*, 100, 2473–2490, https://doi.org/10.1175/BAMS-D-19-0001.1.
- Massmann, A. K., J. R. Minder, R. D. Garreaud, D. E. Kingsmill, R. A. Valenzuela, A. Montecinos, S. L. Fults, and J. R. Snider, 2017: The Chilean Coastal Orographic Precipitation Experiment: Observing the influence of microphysical rain regimes on coastal orographic precipitation. *J. Hydrometeor.*, 18, 2723–2743, https://doi.org/10.1175/JHM-D-17-0005.1.
- Minder, J. R., D. R. Durran, G. H. Roe, and A. M. Anders, 2008: The climatology of small-scale orographic precipitation over the Olympic Mountains: Patterns and processes. *Quart. J. Roy. Meteor. Soc.*, 134, 817–839, https://doi.org/10.1002/qj.258.
- Nakanishi, M., and H. Niino, 2004: An improved Mellor–Yamada level-3 model with condensation physics: Its design and verification. *Bound.-Layer Meteor.*, **112**, 1–31, https://doi.org/10.1023/B:BOUN.0000020164.04146.98.
- Neiman, P. J., F. M. Ralph, A. B. White, D. E. Kingsmill, and P. O. G. Persson, 2002: The statistical relationship between upslope flow and rainfall in California's coastal mountains: Observations during CALJET. *Mon. Wea. Rev.*, 130, 1468-1492, https://doi.org/10.1175/1520-0493(2002)130<1468:TSRBUF>2. 0.CO;2.
- Niu, G.-Y., and Coauthors, 2011: The community Noah land surface model with multiparameterization options (Noah-MP): 1. Model description and evaluation with local-scale measurements.

- J. Geophys. Res., 116, D12109, https://doi.org/10.1029/2010JD015139
- Pokharel, B., and G. Vali, 2011: Evaluation of collocated measurements of radar reflectivity and particle sizes in ice clouds. J. Appl. Meteor. Climatol., 50, 2104–2119, https://doi.org/10.1175/JAMC-D-10-05010.1.
- Prein, A. F., G. J. Holland, R. M. Rasmussen, J. Done, K. Ikeda, M. P. Clark, and C. H. Liu, 2013: Importance of regional climate model grid spacing for the simulation of heavy precipitation in the Colorado headwaters. *J. Climate*, 26, 4848–4857, https://doi.org/10.1175/JCLI-D-12-00727.1.
- Reinking, R. F., J. B. Snider, and J. L. Coen, 2000: Influences of storm-embedded orographic gravity waves on cloud liquid water and precipitation. *J. Appl. Meteor. Climatol.*, **39**, 733–759, https://doi.org/10.1175/1520-0450(2000)039<0733:IOSEOG>2.
- Reisner, J., R. M. Rasmussen, and R. T. Bruintjes, 1998: Explicit forecasting of supercooled liquid water in winter storms using the MM5 mesoscale model. *Quart. J. Roy. Meteor. Soc.*, **124**, 1071–1107, https://doi.org/10.1002/qj.49712454804.
- Roe, G. H., 2005: Orographic precipitation. Annu. Rev. Earth Planet. Sci., 33, 645–671, https://doi.org/10.1146/annurev.earth. 33.092203.122541.
- Serreze, M. C., M. P. Clark, R. L. Armstrong, D. A. McGinnis, and R. S. Pulwarty, 1999: Characteristics of the western United States snowpack from Snowpack Telemetry (SNOTEL) data. *Water Resour. Res.*, 35, 2145–2160, https://doi.org/10.1029/ 1999WR900090.
- Smith, R. B., and I. Barstad, 2004: A linear theory of orographic precipitation. *J. Atmos. Sci.*, **61**, 1377–1391, https://doi.org/10.1175/1520-0469(2004)061<1377:ALTOOP>2.0.CO;2.
- Tessendorf, S. A., and Coauthors, 2019: A transformational approach to winter orographic weather modification research: The SNOWIE project. *Bull. Amer. Meteor. Soc.*, **100**, 71–92, https://doi.org/10.1175/BAMS-D-17-0152.1.
- Thompson, G., and T. Eidhammer, 2014: A study of aerosol impacts on clouds and precipitation development in a large winter cyclone. *J. Atmos. Sci.*, **71**, 3636–3658, https://doi.org/10.1175/JAS-D-13-0305.1.

- University of Wyoming Research Flight Center, 2017a: Flight level data from the University of Wyoming King Air during the Seeded and Natural Orographic Wintertime clouds—the Idaho Experiment (SNOWIE) project, version 1.0. University of Wyoming Dept. of Atmospheric Science, accessed 10 January 2021, https://doi.org/10.15786/M2MW9F.
- —, 2017b: Wyoming Cloud Radar data from the University of Wyoming King Air during the University of Wyoming King Air during the Seeded and Natural Orographic Wintertime clouds—the Idaho Experiment (SNOWIE) project, version 1.0. University of Wyoming Dept. of Atmospheric Science, accessed 10 January 2021, https://doi.org/10.15786/M2CD4J.
- Vali, G., and S. Haimov, 2001: Observed extinction by clouds at 95 GHz. IEEE Trans. Geosci. Remote Sens., 39, 190–193, https://doi.org/10.1109/36.898682.
- Wang, Z., and Coauthors, 2012: Single aircraft integration of remote sensing and in situ sampling for the study of cloud microphysics and dynamics. *Bull. Amer. Meteor. Soc.*, 93, 653–668, https://doi.org/10.1175/BAMS-D-11-00044.1.
- Xue, L., and Coauthors, 2022: Comparison between observed and simulated AgI seeding impacts in a well-observed case from the SNOWIE field program. J. Appl. Meteor. Climatol., 61, 345–367, https://doi.org/10.1175/JAMC-D-21-0103.1.
- Zagrodnik, J. P., L. McMurdie, and R. Conrick, 2021: Microphysical enhancement processes within stratiform precipitation on the barrier and sub-barrier scale of the Olympic Mountains. *Mon. Wea. Rev.*, 149, 503–520, https://doi.org/10.1175/MWR-D-20-0164.1.
- Zaremba, T. J., and Coauthors, 2022a: Vertical motions in orographic cloud systems over the Payette River basin. Part I: Uncertainty in recovery of vertical motions from airborne Doppler radial velocity measurements. J. Appl. Meteor. Climatol., 61, 1713–1731, https://doi.org/10.1175/JAMC-D-21-0228.1
- —, and Coauthors, 2022b: Vertical motions in orographic cloud systems over the Payette River basin. Part II: Fixed and transient updrafts and their relationship to forcing. *J. Appl. Meteor. Climatol.*, **61**, 1733–1751, https://doi.org/10.1175/JAMC-D-21-0229.1.